

UNCLASSIFIED

SECURITY CLASSIFICATION OF THIS PAGE (When Data Entered)

AD A 137007

REPORT DOCUMENTATION PAGE		READ INSTRUCTIONS BEFORE COMPLETING FORM	
1. REPORT NUMBER AFOSR-TR. 83-1315	2. GOVT ACCESSION NO. AD-A137007	3. RECIPIENT'S CATALOG NUMBER	
4. TITLE (and Subtitle) Body and Surface Wave Modeling of Observed Seismic Events		5. PERIOD COVERED <i>1 Nov 80 - 30 Apr 82</i>	
7. AUTHOR(s) David G. Harkrider Donald V. Helmberger	6. PERFORMING ORG. REPORT NUMBER F49620-81-C-0008		
9. PERFORMING ORGANIZATION NAME AND ADDRESS California Institute of Technology Seismological Laboratory, 252-21 Pasadena, California 91125	10. PROGRAM ELEMENT, PROJECT, TASK AREA & WORK UNIT NUMBERS ARPA Order No. 3291.40 61102F 2309/A1		
11. CONTROLLING OFFICE NAME AND ADDRESS AFOSR / VP Building 410 Bolling AFB, D.C. 20332	12. REPORT DATE 1 NOV 1980 - 30 APR 82		
14. MONITORING AGENCY NAME & ADDRESS (if different from Controlling Office)	13. NUMBER OF PAGES 91		
16. DISTRIBUTION STATEMENT (of this Report) Approved for public release; distribution unlimited		15. SECURITY CLASS. (of this report) Unclassified	
17. DISTRIBUTION STATEMENT (of the abstract entered in Block 20, if different from Report)		15a. DECLASSIFICATION/DOWNGRADING SCHEDULE JAN 20 1984	
18. SUPPLEMENTARY NOTES A			
19. KEY WORDS (Continue on reverse side if necessary and identify by block number) Near-field synthetics, tectonic release below NTS, body wave travel time and amplitude anomalies across North America			
20. ABSTRACT (Continue on reverse side if necessary and identify by block number) Cont'd on next pages.			

DD FORM 1 JAN 73 1473

UNCLASSIFIED

SECURITY CLASSIFICATION OF THIS PAGE (When Data Entered)

~~UNCLASSIFIED~~

1

Cont'd. #20

Abstract

AFOSR-TR- 83-1315

I. SUMMARY

The research performed under the contract during the period 1 November 1981 through 30 April 1982 can be divided into two main topics; coupling of surface waves in laterally inhomogeneous source regions to teleseismic propagation paths, and a review of the theory and application of synthetic seismograms.

In Section II, the dimensions of the cylindrical source region and its linear gradient transition zone were varied in order to determine their effect on the generation of teleseismic Rayleigh waves. By comparing amplitudes from a source region with sharp boundaries at the sides and bottom with those from a region bounded by various combinations of sharp and transition boundaries, it was determined that for these source dimensions at the periods of interest, the more the body wave energy that leaves the source region as downgoing waves, the larger the fundamental mode Rayleigh wave.

In Section III, a review on the theory and application of synthetic seismograms is presented. The emphasis is on body phase wave forms at teleseismic, regional, and local epicentral distances. At teleseismic distances, it was shown that long period body phases from shallow earthquakes are coherent at neighboring stations and that the observed waveform could be decomposed in a manner that allows determination of faulting parameters. By modeling both long and short period body waveforms

~~UNCLASSIFIED~~

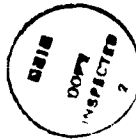
UNCLASSIFIED

Cont'd. #20

Abstract

AFOSR-TR-83-1315

using distributed point sources it is found that most earthquakes are indeed complex and that high frequency strong motions appear to be more strongly controlled by the jumps in the source time history than by the overall duration. At ranges less than 30°, body wave arrivals become multi-valued and some care needs to be taken to remove propagation features from source phenomenon.



UNCLASSIFIED

AFOSR-TK-83-1315

FINAL

**TECHNICAL REPORT
1 November 1981 - 30 April 1982
*(1980)***

ARPA Order No.: 3291.40
Program Code: 1A10
Name of Contractor: California Institute of Technology
Effective Date of Contract: 1 November 1981
Contract Expiration Date: 31 October 1982
Amount of Contract: \$199,997
Contract Number: F49620-81-C-0008
Principal Investigators:
David G. Harkrider
(213) 356-6910
Donald V. Helmberger
(213) 356-6911
Program Manager and Telephone Number: William J. Best
(202) 767-5011
Short Title of Work: Body and Surface Wave Modeling
of Observed Seismic Events

The views and conclusions contained in this document are those of the authors and should not be interpreted as necessarily representing the official policies, either expressed or implied, of the Defense Advanced Research Projects Agency or the U.S. Government.

Sponsored by
Advanced Research Projects Agency (DOD)
ARPA Order No. 3291.40
Monitored by AFOSR Under Contract No. F49620-81-C-0008

Seismological Laboratory
Division of Geological and Planetary Sciences
California Institute of Technology
Pasadena, California 91125

84 01 19 072

Approved for public release;
distribution unlimited.

A

TABLE OF CONTENTS

	Page
I. Summary.	1
II. Representation theorem modeling of Rayleigh waves from laterally inhomogeneous source regions.	3
III. Theory and application of synthetic seismograms. .	16

1 AIR FORCE OFFICE OF SCIENTIFIC RESEARCH
NOTICE OF PUBLIC RELEASE
Title: Rayleigh
Author: J. R. Gough
Distribution: Uncontrolled
MATTHEW J. KLEINER
Chief, Technical Information Division

I. SUMMARY

The research performed under the contract during the period 1 November 1981 through 30 April 1982 can be divided into two main topics: coupling of surface waves in laterally inhomogeneous source regions to teleseismic propagation paths, and a review of the theory and application of synthetic seismograms.

In Section II, the dimensions of the cylindrical source region and its linear gradient transition zone were varied in order to determine their effect on the generation of teleseismic Rayleigh waves. By comparing amplitudes from a source region with sharp boundaries at the sides and bottom with those from a region bounded by various combinations of sharp and transition boundaries, it was determined that, for these source dimensions at the periods of interest, the more the body wave energy that leaves the source region as downgoing waves, the larger the fundamental mode Rayleigh wave.

In Section III, a review on the theory and application of synthetic seismograms is presented. The emphasis is on body phase wave forms at teleseismic, regional, and local epicentral distances. At teleseismic distances, it was shown that long period body phases from shallow earthquakes are coherent at neighboring stations and that the observed waveform could be decomposed in a manner that allows determination of faulting parameters. By modeling both long and short period body waveforms

using distributed point sources it is found that most earthquakes are indeed complex and that high frequency strong motions appear to be more strongly controlled by the jumps in the source time history than by the overall duration. At ranges less than 30°, body wave arrivals become multi-valued and some care needs to be taken to remove propagation features from source phenomenon.

II

**Representation Theorem Modeling of Rayleigh
Waves from Laterally Inhomogeneous Source Regions**

by

Peter Glover and David G. Harkrider

INTRODUCTION.

During the past year, we have examined the effectiveness of two mixed-path surface wave algorithms previously used to couple various source region models to a common propagation path. Rayleigh waves generated by the two algorithms were compared to the more numerically accurate Representation Theorem technique of modeling which couples finite element code results of a source in a laterally inhomogeneous region to the laterally homogeneous propagation path. The principal advantage of the two approximations is that they are computationally economic and require only trivial modifications to existing Rayleigh wave codes. On the other hand, the RT technique is relatively expensive depending on the frequencies or wavelengths desired from the finite element/finite difference code modeling the transition zone. Since changing the source region structure and radius for each case of interest would require further FE/FD code calculations, we had hoped that at least one of the two mixed path techniques would be adequate for obtaining Green's functions for Rayleigh waves generated in complex source regions.

In our semi-annual report for November, 1981 we showed that for the case where the propagation medium was a uniform halfspace, the

Conservation of Lateral Energy Flux (CLEF) method gave better agreement with the RT result than the Unit Transmission Coefficient (UTC) method when the source region was modeled by a cylinder of radius 1.8 km and height 1.8 km embedded in the propagation medium. The material properties of this cylinder were chosen to closely approximate those of two typical NTS source media, Climax Stock granite and Yucca Flat tuff (see Table 1). These results are reproduced in Figure 1. Figure 2 shows a similar calculation for the case where the propagation medium was CIT109, a model frequently used to calculate surface wave propagation in the western U.S. Together, these figures show that for the Climax Stock model, where the source/receiver rigidity ratio is 0.6, both approximations agree with the RT results. However, for the Yucca Flat model, where the rigidity ratio is 0.1, the CLEF method is the better approximation.

The results given in Figures 1 and 2 are for a sharp boundary. In this report we examine the effects of gradational boundaries, keeping essentially the same source region geometry and using a vertical point-force source at a depth of 0.4 km. For the Yucca Flat tuff source region model, we find that a gradational boundary on the bottom of the cannister gives the largest Rayleigh waves. However, the maximum peak-to-peak amplitude is 6.0×10^{-21} cm compared to 3.5×10^{-21} cm for a similar force of 1 dyne in the laterally homogeneous model CIT109.

EFFECTS OF GRADATIONAL BOUNDARIES.

Figure 3a shows the RT and CLEF results for the sharp 1.8×1.8 km

Yucca model plotted on a common scale. The maximum peak-to-peak amplitude is 3.9×10^{-21} cm for the CLEF method compared to 4.0×10^{-21} cm for the RT method. The associated periods are 15 and 12 seconds respectively. The CLEF approximation underestimates the amplitudes at 25 second periods. At 3 to 5 second periods, the two methods disagree in both amplitude and phase. Nevertheless, overall the CLEF approximation is in good agreement with the RT result.

The underlying assumption of the CLEF method is that the horizontal energy flux transported in the fundamental mode Rayleigh wave on the left of the boundary is equal to that in the fundamental mode Rayleigh wave on the right of the boundary. That is, there is no energy loss due to mode conversions, or reflections. This is not true for the finite element calculations of the forcing functions. ζ_{SES} was deliberately chosen to be in the propagation region in order to monitor the change in wavefield between the source region and the the propagation medium. For the high impedance contrast Yucca model, the outgoing wavefield should experience significant reflections and conversions on encountering the sharp boundary of the cannister. Therefore, we would expect the CLEF approximation to give an even closer agreement with a RT model incorporating an impedance gradient.

To investigate this effect, we introduced a series of stepwise increases in velocity and density across the 3 columns/rows of elements forming the RHS/bottom of the plug. The radius/height was also increased to 2.0 km to accomodate this gradient. However, ζ_{SES} was maintained at $r = 2.1$ km, $z = 2.1$ km through these runs. Figure 3b

shows the results for a "uniform" gradient across the RHS of the plug compared to the CLEF result for the sharp 1.8×1.8 km plug. In this case, the RT results have a peak-to-peak amplitude of $3.3 \times 10^{**-21}$ cm, compared to $3.9 \times 10^{**-21}$ cm for the CLEF results. The minimum value in the CLEF result is delayed by approximately 3 seconds with respect to the RT result. However, the two methods give nearly the same result at the longer periods. This is not due to the presence of the gradient reducing the effective radius of the sharp boundary, as can be seen from Figure 3c. In fact, when we compare the effect of plug radius on the results using the RT method alone (Figure 4a), it is clear that such small perturbations have no measurable effect. Therefore, the presence of the gradient must be diminishing the signal amplitudes by suppressing reflections from the side of the plug. This is further demonstrated in Figure 4c, where the RT result for the gradient model shows smaller amplitudes at all frequencies than the RT result for the sharp boundary, and an 18 percent decrease in the maximum peak-to-peak value.

Using a plug of height 2.0 km and radius 1.8 km, we incorporated the same velocity and density gradient across the bottom of the cannister. Figure 4b shows the new result compared to the RT method for the sharp plug. The gradient gives larger amplitudes at all but the shortest periods and the peak-to-peak maximum is $6.0 \times 10^{**-21}$ cm or 50 percent larger than the sharp boundary. Moreover, there is little difference in phase between the two results.

We also computed the Rayleigh wave for a gradient on both the bottom and the side of the plug. These results are shown in Figure 5.

In this case, the peak-to-peak amplitude is 5.2×10^{-21} cm, somewhat smaller than that of the bottom only gradient, but still significantly larger than for the sharp boundary. At other periods, the sharp vs gradational results are in good agreement. Finally, Figures 5b and 5c compare the totally surrounded plug with the previous cases. The important thing to note is that the gradient across the bottom of the plug has the largest effect on the peak-to-peak amplitude of the computed Rayleigh wave signatures.

DISCUSSION.

The observation that the maximum amplitudes come from the source region model with velocity gradient at depth can be explained as follows. The effect of the sharp boundary on the side of the cannister is to reflect rays at non-normal angles of incidence so that they eventually impinge on the bottom surface of the cannister. Here the contributions due to the normal stresses are a factor of 2 larger than those for the side. This implies that, for the periods of interest here, the more body wave energy that leaves the source region as downgoing waves, the larger the fundamental mode Rayleigh wave. The gradient itself acts so as to minimize reflections from the bottom of the cannister. The results from the gradient on both bottom and side are consistent in that the peak amplitudes are somewhat less than the case of the gradient across the bottom, but greater than those for the sharp case. When the gradient occurs only on the side, the results are smaller than for the sharp boundary, which is consistent. Moreover, the

results for this case most nearly match the CLEF results, although at the distances involved the energy is being transported across the impedance contrast as body waves and static deformations, rather than as fundamental mode surface waves (see Harkrider, 1981 for a derivation of the CLEF approximation).

So, although our results with these spatially limited source regions clearly indicate that, when observed with a long-period LRSM-type instrument, effects of lateral heterogeneity can be modeled to first order using the CLEF approximation, we cannot offer a detailed explanation as to why.

REFERENCE

Harkrider, D. G., Coupling near source phenomena into surface wave generation; Identification of Seismic Sources - Earthquake or Underground Explosion, ed. E. S. Husebye and S. Mykkeltveit, D. Reidel Publishing Co., Boston, pp. 277-326, 1981.

Table 1
Layer parameters for the Climax Stock and Yucca Flat models

	α	β	ρ	μ
Yucca Flat Tuff	2.35	1.3	1.86	3.14
Climax Stock Granite	5.33	2.78	2.67	20.63
CIT109 (Upper 14 km)	6.2	3.511	2.736	33.73

FIGURE CAPTIONS.

Figure 1. Comparison of mixed path results at 1200 km; source medium 1.8×1.8 km right cylinder, sharp boundaries; propagation medium uniform halfspace $\alpha = 6.2$ km/sec, $\beta = 3.5$ km/sec, $\rho = 2.7$ gm/cc. Both approximations overestimate high frequencies.

Figure 2. Similar calculations for layered propagation medium. UTC result for Yucca Flat tuff still dominated by high frequencies.

Figure 3. From top to bottom, RT results for a) sharp boundaries, b) gradational boundary on side, c) sharp boundaries but reduced radius, superimposed on CLEF result with maximum and minimum amplitudes of 2.0 and -2.2×10^{-21} cm.

Figure 4. RT results for a) source region radius 1.6 km, b) gradational boundary across bottom, c) across side, superimposed on RT result for sharp 1.8×1.8 km source region, peak-to-peak amplitude 4.0×10^{-21} cm.

Figure 5. RT results for a) sharp 1.8×1.8 km source region, b) gradational boundary across side, c) across bottom, compared to totally gradational case, peak-to-peak amplitude 5.2×10^{-21} cm.

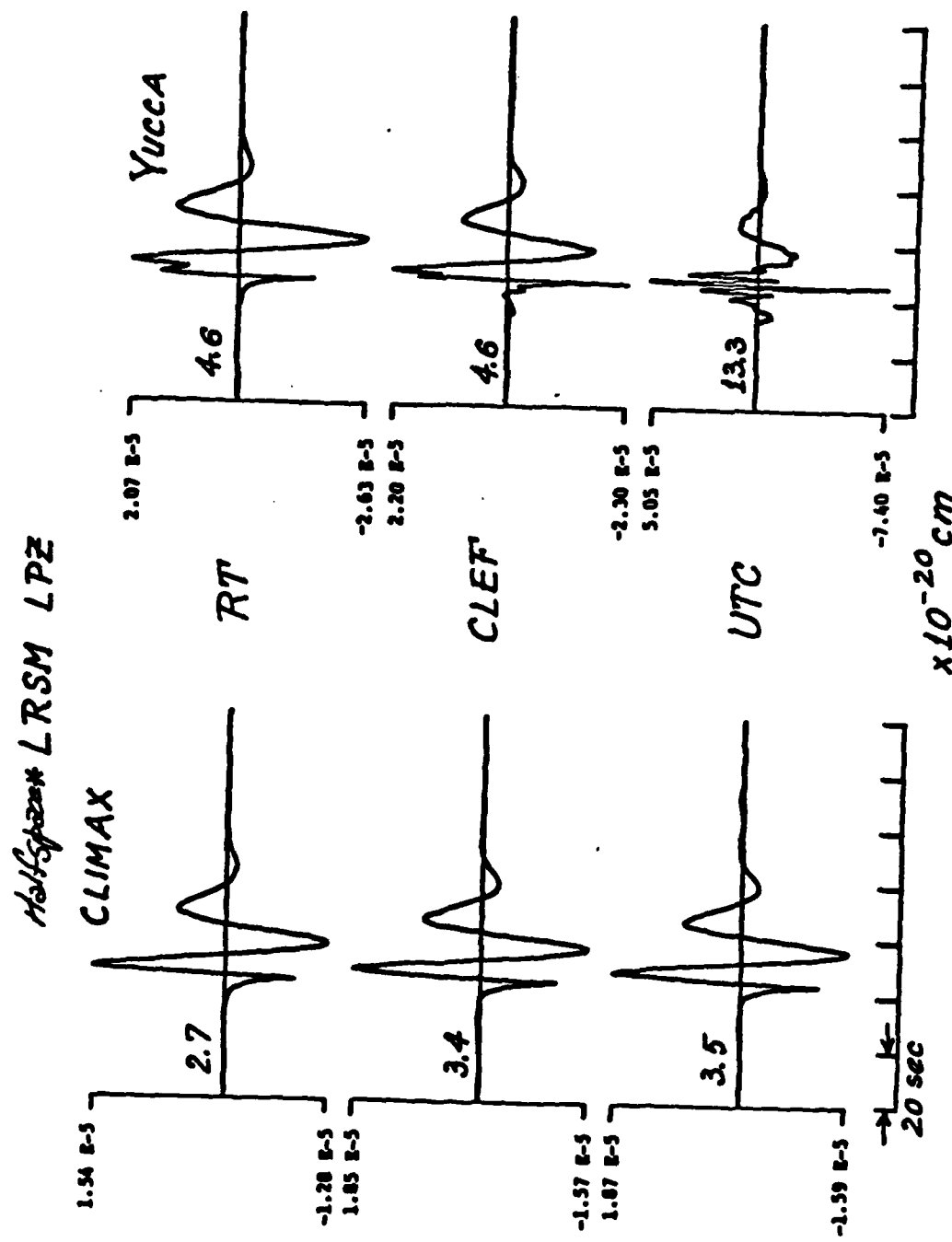


Figure 1

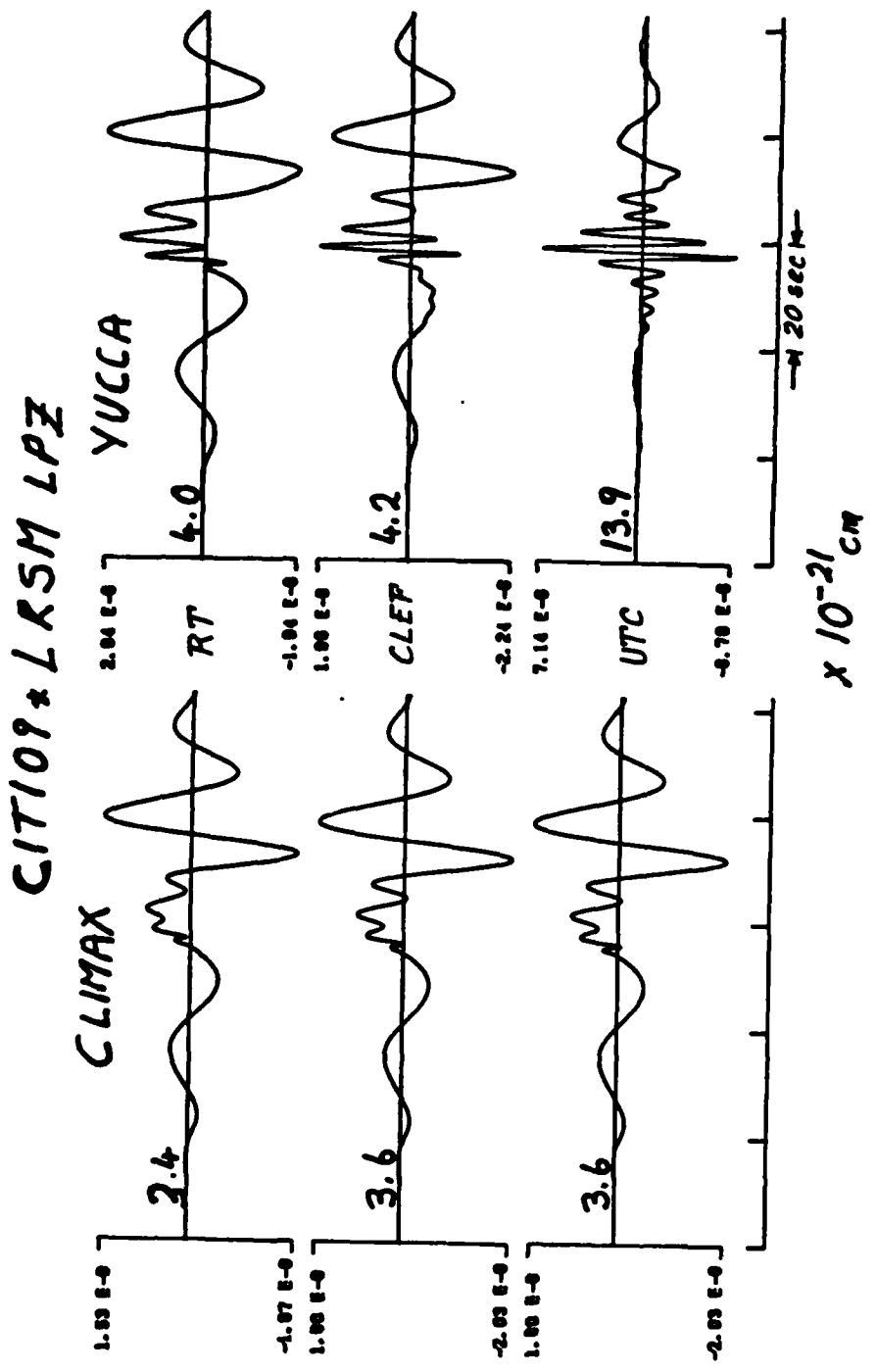


Figure 2

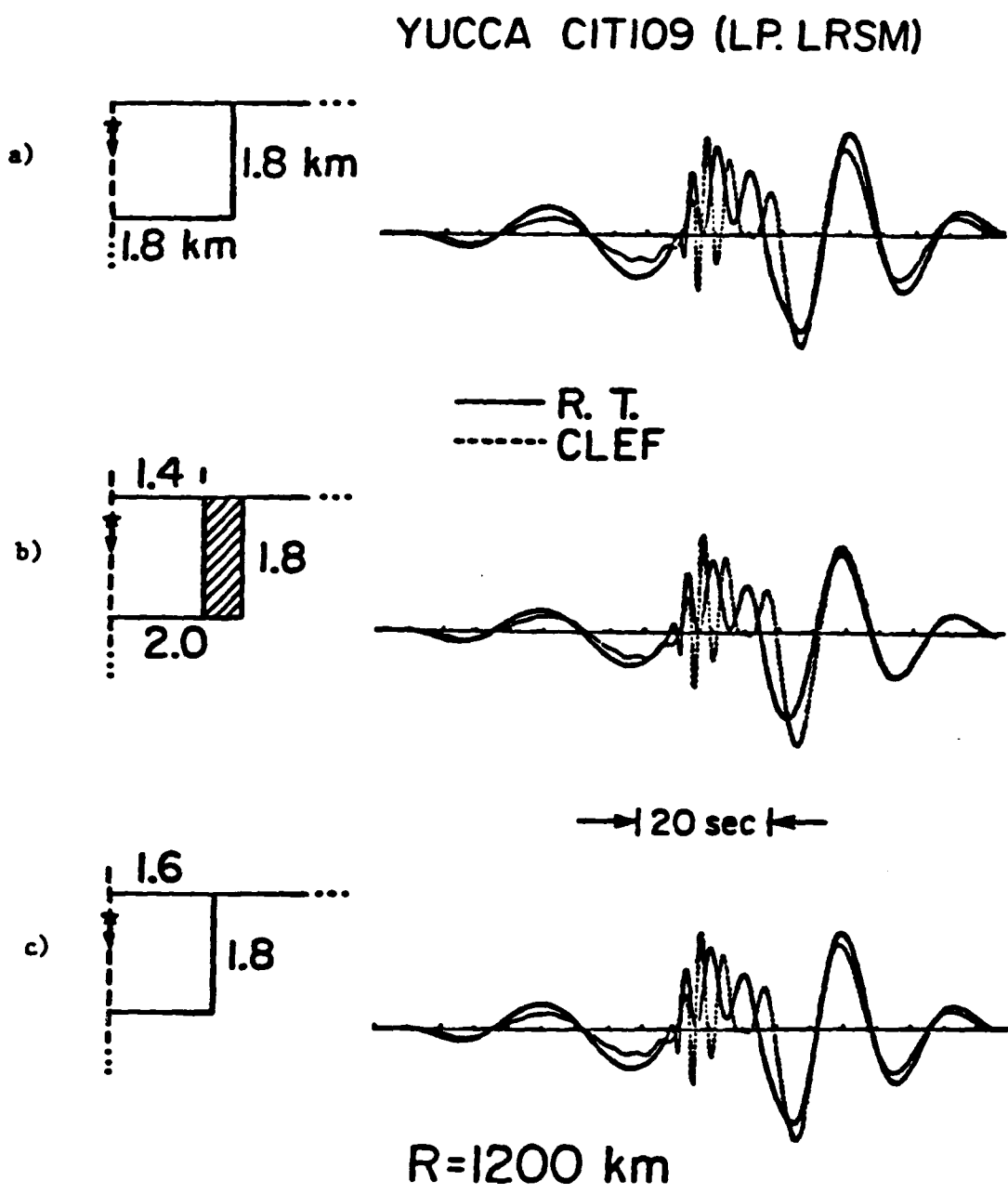


Figure 3

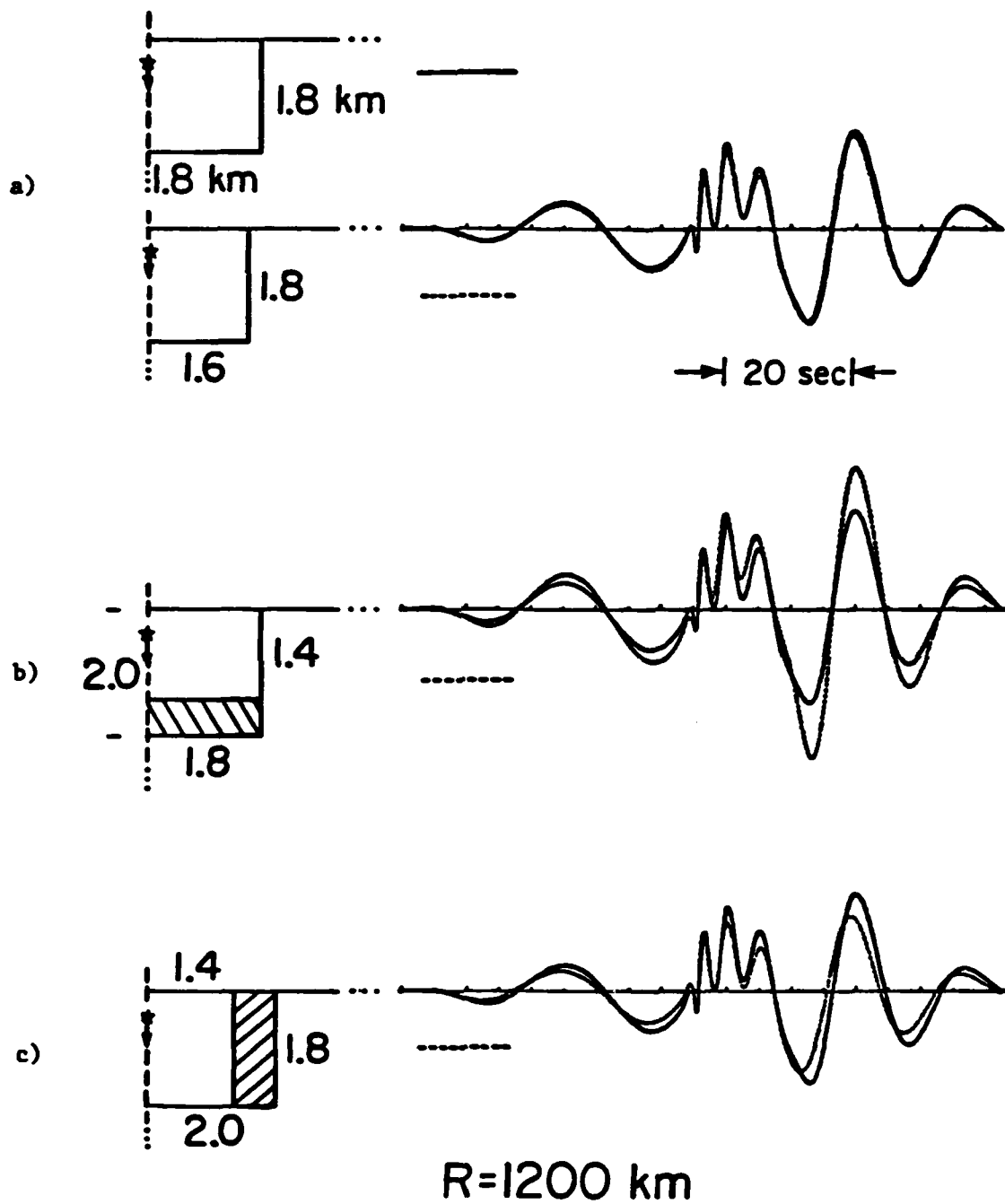


Figure 4

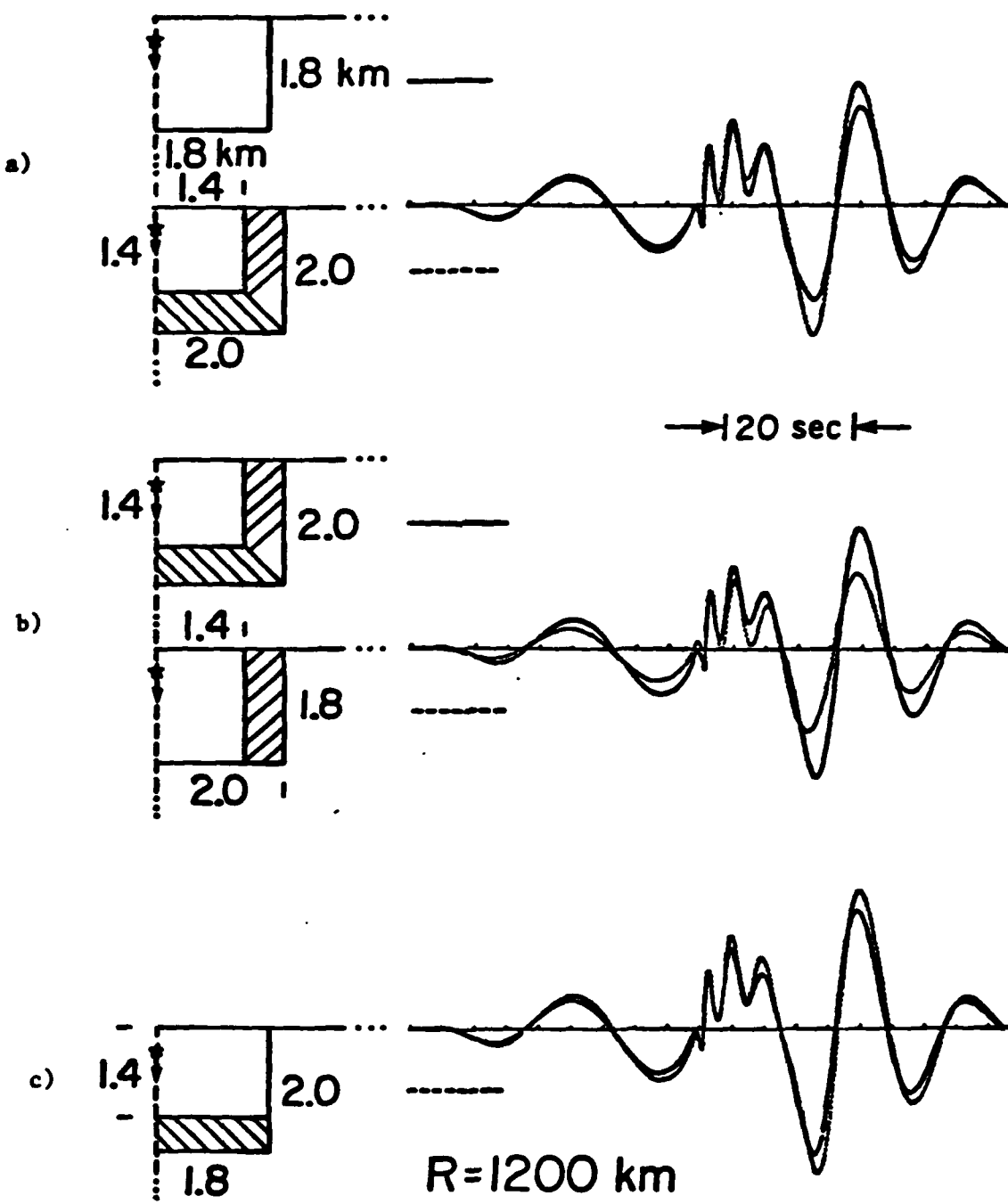


Figure 5

III

THEORY AND APPLICATION OF SYNTHETIC SEISMOGRAMS

Don V. Helmberger

**Seismological Laboratory, 252-21
California Institute of Technology
Pasadena, California 91125**

May 26, 1982

1. Introduction

In the past decade, our understanding of earthquakes and earth structure has increased significantly based on our improved ability to interpret seismograms. Numerous formalisms have been developed whereby synthetic seismograms can be computed at positions on the earth for comparisons with observed seismograms. The various processes that affect the motion at some field point such as the seismic source, earth model response, attenuation and recording equipment are all combined into the synthetic convolution operators. Since these effects can be treated as linear operators to first order it becomes simple to test the significance of changes in the synthetics caused by varying the operators separately. By comparing the synthetic with observed seismograms we can apply iterative techniques to determine earth structure or source model, or perhaps some properties of each depending on the circumstances. Applications of this procedure to body waves have proven quite effective in determining the source properties of shallow earthquakes. We shall review these studies in some detail in this set of notes.

There are four basic operators which are generally included in the generation of synthetics. These represent the seismic instrumental response, $I(t)$, the attenuation operator, $A(t)$, the source operator, $S(t)$, and a wave propagation operator or Green's function, $M(t)$. The synthetic seismogram, $SS(t)$, is computed by the triple convolution

$$SS(t) = I(t) * A(t) * M(t) * S(t)$$

where the first of these is generally well known.

We will be primarily interested in events recorded by the World Wide Seismic System Network (WWSSN). This global network of stations is displayed in Figure 1.1. Each station records three components of motion, namely vertical, north-south, and east-west, on photographic paper. Because the earth is particularly noisy at about 4 sec, it is convenient to record each component in two pass-bands, short period (SP) and long period (LP). The gains or amplifications of (SP's) are normally between 25 to 200 thousand while the (LP's) run at 750 to 3000.

The attenuation operator does not introduce any structure into the waveforms in most problems of interest but only smooths the results. The operator which is most commonly used could be more properly written $A(t, t^*)$ where $t^* = \int ds/Q$ where Q is the quality factor and the integration is performed along the path of the ray, see Carpenter (1967) and Futterman (1962). Most recent estimates of t^* are near 1 for P-waves and 4 or larger for shear waves assuming shallow events. The effects of the attenuation operator convolved with the instrumental responses are displayed in Figure 1.2. Note that for a t^* of (4) the short periods are greatly reduced. Thus, we should not expect to see short-period shear waves from shallow sources which is generally true. There is considerable evidence for a frequency dependent attenuation operator, particularly at the high frequencies (say > 3 hz), see Minster (1978). We will be primarily interested in the long-period seismograms and will apply the $A(t^*, t)$ for simplicity.

Calculating $M(t)$ can be quite simple or complex depending on circumstances and epicentral distances. At teleseismic distances, 30°

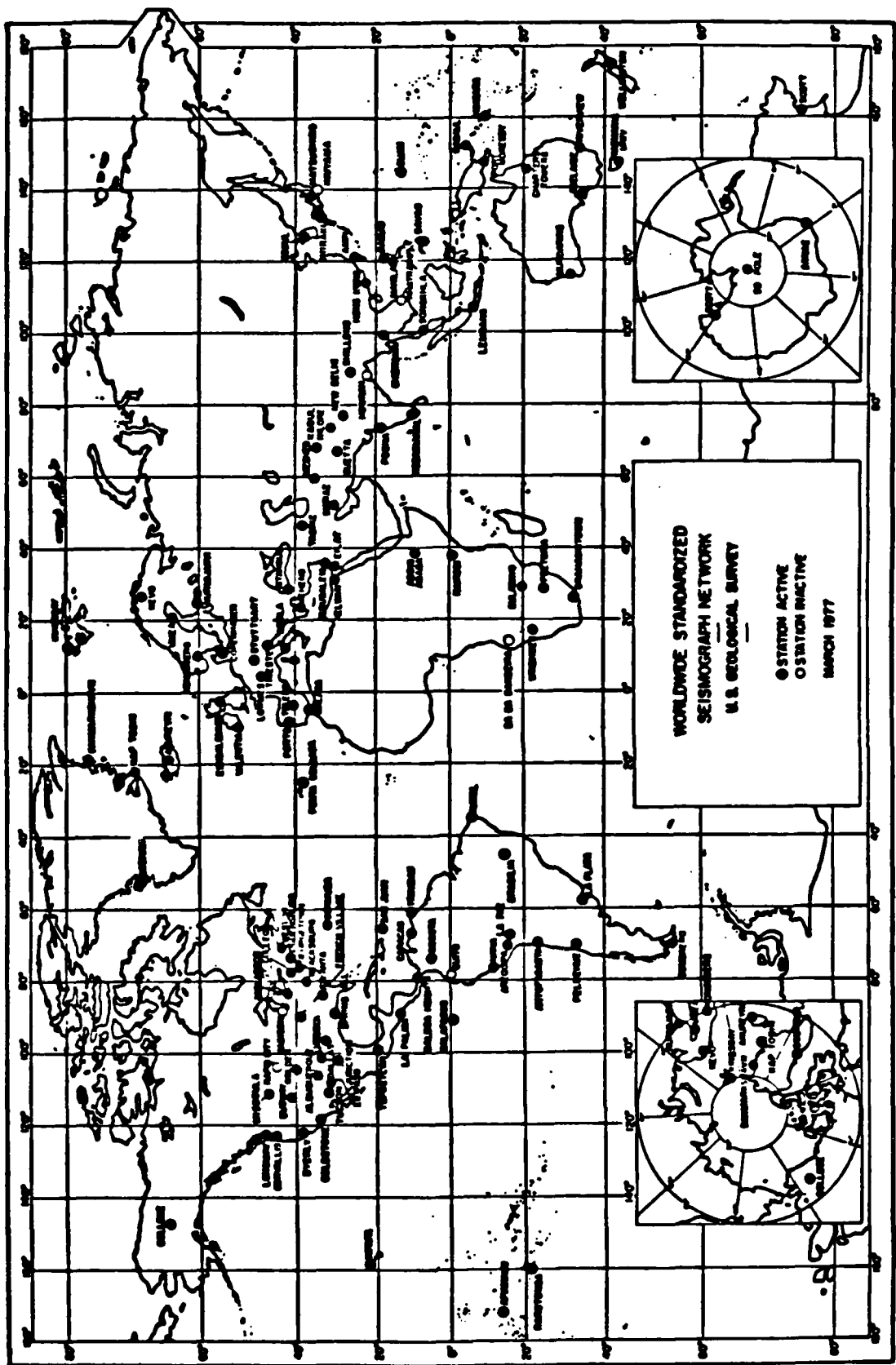


Fig 1.1 - WSSN global network
(after USGS).

Fig 1.2 - The first column displays $A(t, t^*)$ as a function of t^* assuming 0.5, 1.0, 1.5, and 4, from top to bottom. The middle column displays the convolution of $A(t, t^*)$ with the short period instrumental response, and similarly for the long period on the right. The relative amplitudes are indicated by the numbers above each trace.

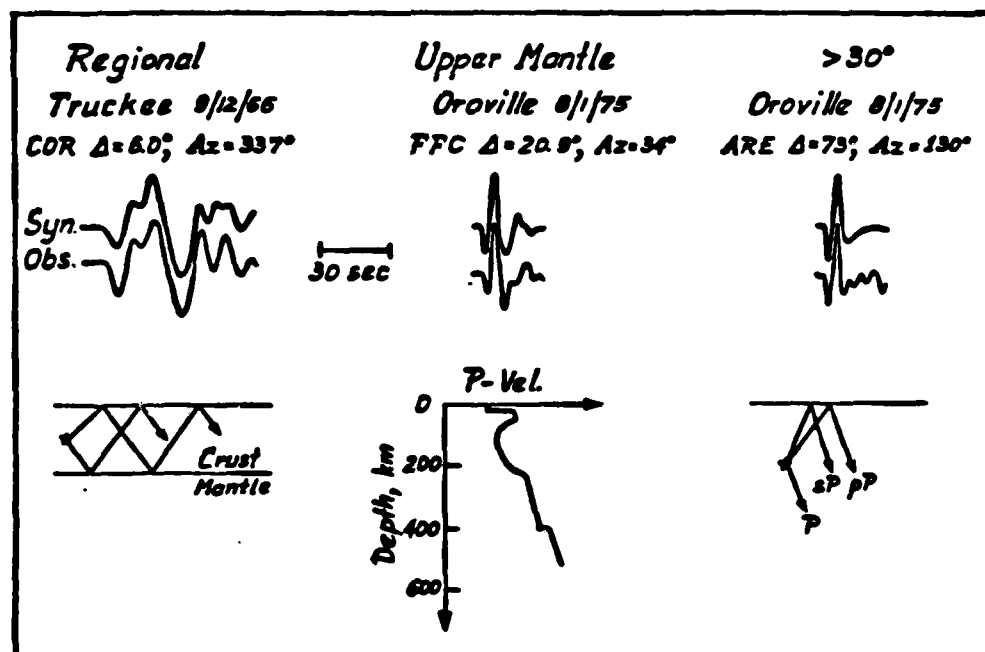
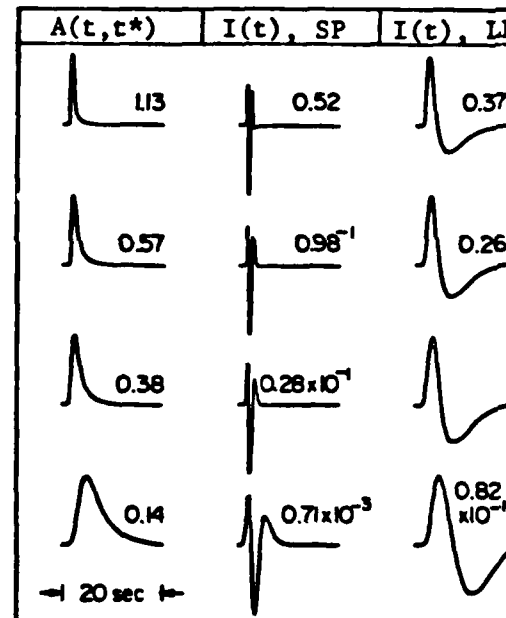


Fig 1.3 - Example observations and synthetics at ranges where the earth appears simple ($> 30^\circ$), slightly complicated (upper-mantle ranges, 30° to 14°), and quite complicated (less than 14°).

to 90° , we can assume that $M(t)$ is a delta function and the only remaining complexity is due to surface reflections, see Figure 1.3. From about 12° to 30° , the earth's upper-mantle triplications introduce additional frequency dependent arrivals making $M(t)$ more interesting. At smaller ranges, the crust plays a more important role and the guided waves following the P-wave prove quite useful. Methods for generating $M(t)$ abound and their descriptions are covered in great detail in any of the recent textbooks. In this set of notes, we will apply generalized ray theory, GRT, and the Cagniard-de Hoop formalism since the author is the most familiar with this technique and it can be used effectively at all ranges.

2. Source descriptions and generalized ray theory

The seismic radiation field produced by earthquakes can be represented by several means. Following the stress relaxation approach, one assumes the initial stress and frictional conditions and performs the proper dynamics using analytical or numerical techniques to obtain the displacements, see for example Madariaga (1976). Another particularly useful approach is due to Haskell (1964), called the shear-dislocation model. Following this approach one does not attempt to understand the detailed mechanics involved in the actual fault zone but simply states that slip occurs on a specified surface, referred to as a dislocation.

However, before getting into the substantial complexities involved in the shear dislocation formalism it appears useful to review a much simpler spherically symmetric source or an idealized point source

explosion.

a) Symmetric Point Source

We assume a homogeneous fluid with cylindrical coordinates r and z , see Figure 2.1. This choice of coordinates will prove advantageous for studying a layered earth in later considerations. We will, also, take this opportunity to develop some mathematical tools which will prove useful. The wave equation in cylindrical coordinates with no azimuthal dependence is

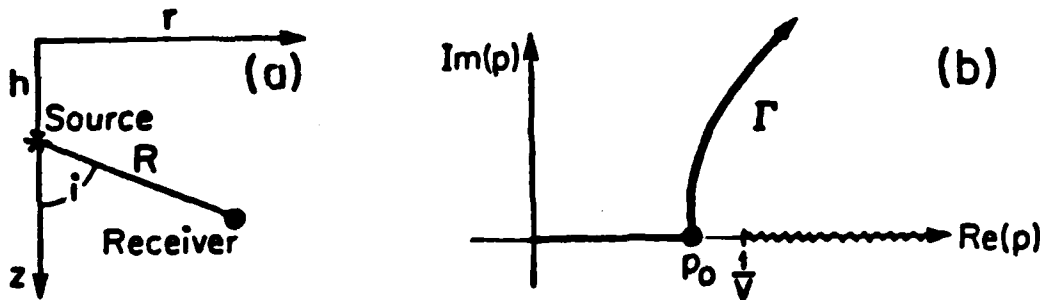


Fig 2.1 - Source-receiver geometry (a) and complex (p) plane (b) with branch cut starting at $(1/V)$ and running out along the real (p) axis.

$$(2.1) \quad \frac{d^2\phi}{dr^2} + 1/r \frac{d\phi}{dr} + \frac{d^2\phi}{dz^2} - 1/a^2 \frac{d^2\phi}{dt^2} = 0$$

where (ϕ) is the displacement potential and (a) the compressional velocity. Taking the Laplace transform of (2.1) yields

$$(2.2) \quad \frac{d^2\bar{\phi}}{dr^2} + 1/r \frac{d\bar{\phi}}{dr} + \frac{d^2\bar{\phi}}{dz^2} - s^2/a^2 \bar{\phi} = 0$$

where (s) is the Laplace transform variable. A solution of (2.2) which is easily demonstrated by substitution is

$$(2.3) \quad \bar{\phi}(r, z, s) = J_0(kr)e^{\pm iVz}$$

where (k) is the horizontal wave number, $v = (k^2 + s^2/a^2)^{1/2}$, and J_0 the zero order Bessel function. A more general expression is

$$(2.4) \quad \bar{\phi}(r, z, s) = \bar{f}(s) \int_0^\infty J_0(kr) [A(k)e^{-vz}] dk$$

where we take the positive square root of (v) and consider the solution which converges for large z . The functions $A(k)$ and $\bar{f}(s)$ are arbitrary with respect to the operations in (2.2).

In the vicinity of the source the displacement potential must satisfy the known behavior of a spherical wave which is

$$(2.5) \quad \begin{aligned} \phi_s &= \\ &\begin{cases} 0 & r < R/a \\ 1/R f(r - R/a) & r > R/a \end{cases} \end{aligned}$$

Taking the Laplace transform of (2.5) yields

$$(2.6) \quad \bar{\phi}_s(R, s) = 1/R e^{-(s/a)R} \bar{f}(s)$$

The question now is can we find a way to match this condition (2.6) with the wave solution (2.4) in terms of $\phi(r, z, s)$. This can be accomplished by using a trick originated by Lamb (1904). The needed identity is

$$(2.7) \quad \frac{e^{-\frac{s}{a}R}}{R} = \int_0^\infty J_0(kr) e^{-v|z-b|} \frac{k}{v} dk$$

which is easily proven with the aid of the Fourier-Bessel theorem. This equation is sometimes referred to as the Sommerfeld integral

representation. Thus, the solution in cylindrical coordinates for an arbitrary time history, $f(s)$, becomes

$$(2.8) \quad \bar{\phi}(r, z, s) = \bar{f}(s) \int_0^\infty J_0(kr) e^{-sv|z-h|} \frac{k}{v} dk$$

Of course, the inverse Laplace transform of (2.8) must yield the (2.5) description. We will produce this result by performing the so-called Cagniard-de Hoop transformation, a technique that proves useful in the layered earth model. We make a change of variable $k = -isp$ which transforms Bessel functions to modified Bessel functions, namely

$$(2.9) \quad J_0(-ispr) \rightarrow i/\pi K_0(spr) - i/\pi K_0(-spr)$$

The solution becomes, after Strick (1959),

$$(2.10) \quad \bar{\phi}(r, z, s) = -i \frac{f(s)s}{\pi} \int_{-i+\delta}^{+i+\delta} K_0(spr) e^{-sn|z-h|} \frac{pd\eta}{\eta}$$

where $\eta = (1/a^2 - p^2)^{1/2}$.

This expression can be further simplified by noting the symmetry across the real (p) axis (Schwarz principle of reflection) obtaining

$$(2.11) \quad \bar{\phi}(r, z, s) = f(s) \frac{2}{\pi} \text{Im} \int_{\delta}^{i+\delta} K_0(spr) e^{-sn|z-h|} \frac{pd\eta}{\eta}$$

Equation 2.11 can be solved exactly but there are some useful

approximations to discuss. Using the asymptotic expansion (9.7.2 Abramowitz and Stegun) we have

$$(2.12) \quad K_n(x) = \left(\frac{\pi}{2x}\right)^{1/2} e^{-x} \left[1 + \frac{(n-1)}{8x} + \frac{(n-1)(n-9)}{2(8x)^2} + \dots \right]$$

where $n = 4n^2$. Keeping the first term only we obtain

$$(2.13) \quad \bar{\psi}(r, z, s) = \sqrt{\frac{2}{\pi r s}} \frac{f(s)}{s} \text{Im} \int_0^{1/s} \frac{\sqrt{p}}{\eta} e^{-s(pr+n|z-h|)} dp$$

For simplicity suppose we assume that $f(s) = 1/s$ or that the original source time history is a step function. The delta function response can be determined later by taking a time derivative and the response for an arbitrary source by convolution. The type of integral occurring in (2.13) occurs often in generalized ray theory and it appears worthwhile to discuss a rather ingenious trick for obtaining its solution, see de Hoop (1960). From line source theory we have

$$(2.14) \quad \bar{\psi}(r, z, s) = \text{Im} \int_0^{1/s} e^{-s(pr+n|z-h|)} \frac{dp}{\eta}$$

Note that this integral looks much like the formal definition of the Laplace transform, namely

$$\bar{g}(s) = \int_0^{\infty} e^{-st} g(t) dt$$

This identification leads one to the following change of variable,

$$(2.15) \quad t = pr + (1/a^2 - p^2)^{1/2} |z-h|$$

Solving for $p(t)$ by applying the quadratic formula we obtain

$$(2.16) \quad p = (\pi/R^2)t - (R^2/a^2 - t^2)^{1/2} |z-h|/R^2 \quad (t < R/a)$$

$$\eta = |z-h|/R^2 t + (R^2/a^2 - t^2)^{1/2} x/R^2$$

and

$$(2.17) \quad p = (\pi/R^2)t + i(t^2 - R^2/a^2)^{1/2} |z-h|/R^2 \quad (t > R/a)$$

$$\eta = |z-h|t/R^2 - i(t^2 - R^2/a^2)^{1/2} x/R^2$$

Taking the derivative of (2.16) we obtain

$$(2.18) \quad \frac{dp}{dt} = \frac{\pi}{R^2} + i \left(t^2 - \frac{R^2}{a^2} \right)^{-1/2} \frac{|z-h|t}{R^2} = \frac{i\eta}{\left(t^2 - \frac{R^2}{a^2} \right)^{1/2}}$$

and, similarly, from (2.17)

$$(2.19) \quad \frac{dp}{dt} = \frac{\pi}{R^2} + \left(\frac{R^2}{a^2} - t^2 \right)^{-1/2} \frac{|z-h|t}{R^2} = \frac{\eta}{\left(\frac{R^2}{a^2} - t^2 \right)^{1/2}}$$

We now perform the integration in the "p" plane such that "t" will be positive and real. Such a path is given in Figure 2.1b. The contour (C) that runs, say along the imaginary axis slightly to right of the origin, from (0) to ($i\infty$) is deformed by analytic continuation to the above contour Γ . The contribution from the arc at (∞) is zero and there are no enclosed poles. Thus,

$$(2.20) \quad \bar{\psi}(r, z, s) = \operatorname{Im} \int_C e^{-s(pr + \eta|z-h|)} \frac{dp}{\eta}$$

and

$$= \int_0^\infty e^{-st} \operatorname{Im} \left(\frac{1}{n} \frac{dp}{dt} \right) dt$$

$$\Psi(r, z, t) = \operatorname{Im} \left(\frac{1}{n} \frac{dp}{dt} \right) = \frac{H(t - R/a)}{(t^2 - R^2/a^2)^{1/2}}$$

where $H(t)$ indicates the step function.

Returning to (2.13), with $f(s) = 1/s$, we obtain

$$(2.21) \quad \Phi(r, z, t) = \sqrt{2/r} \frac{1}{\pi} [1/\sqrt{t} * J(t)]$$

where

$$J(t) = \operatorname{Im} \left(\frac{\sqrt{p}}{n} \frac{dp}{dt} \right)$$

and we have used

$$\mathcal{L}(1/\sqrt{t}) = \sqrt{1/\pi s}$$

The convolution operation indicated in (2.21) can be written

$$\int_0^t (t - \tau)^{-\frac{1}{2}} J(\tau) d\tau$$

which can be evaluated either analytically or numerically, depending on the complexity of $J(t)$. In this simple case, we can use the first-motion approximation (Knopoff and Gilbert 1959) and obtain

$$\begin{aligned} J(\tau) &= \sqrt{p} (\tau^2 - R^2/a^2)^{-\frac{1}{2}} H(\tau - R/a) \\ &= \sqrt{\pi/2} \frac{1}{R} (\tau - R/a)^{-\frac{1}{2}} \end{aligned}$$

and

$$\int^t (t-\tau)^{-1/2} (\tau-R/a)^{-1/2} d\tau = \pi H(t - R/a) .$$

Thus, equation (2.21) reduces to

$$\phi(x, z, t) = \frac{1}{R} H(t - R/a)$$

as it must; see Strick (1959) for more details. This operation is easily visualized by performing the convolution by graphical means, see Figure 2.2. Note that one simply multiplies the two functions together and sums from (0) to (t). The answer remains zero until (t) reaches ($t = R/a$) where the two square root singularities overlap and generate a step.

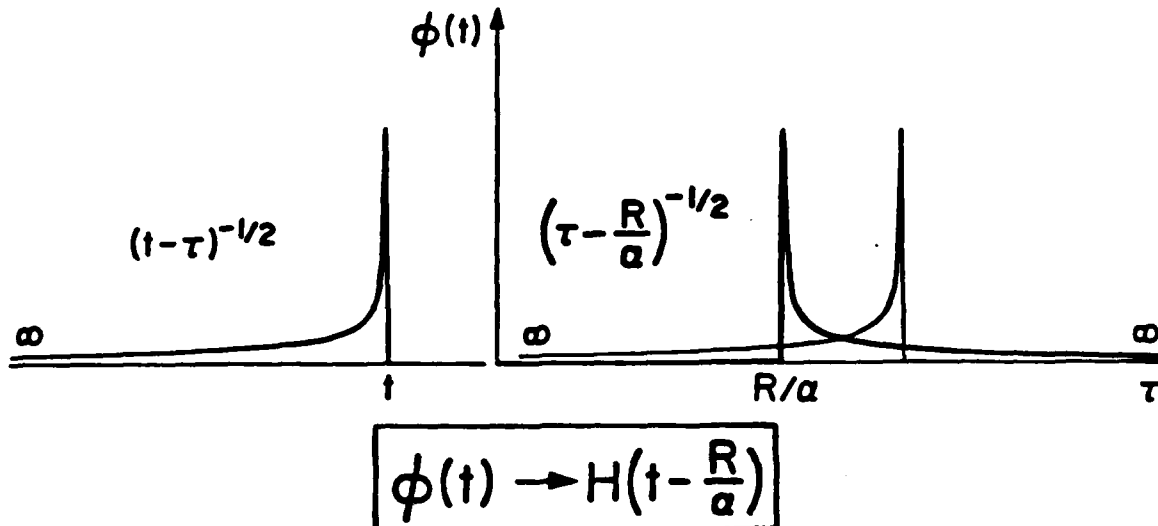


Fig 2.2 - Schematic diagram explaining the convolution operation by graphical means. We reverse the direction of the square-root operation and perform the multiplication of the two functions for values of τ from (0) to (t) and sum. The results are zero until the two functions overlap.

The solutions for more complicated models can be easily obtained with this technique. For instance, suppose we generate the step response appropriate for the interface problem (see Figure 2.3). There will be two generalized rays in the upper halfspace required to solve the boundary conditions, see for instance Spencer (1960) or Helmberger (1968). There will be a direct generalized ray which is identical to the response just discussed plus a generalized ray that describes the response returning from the interface. The latter response can be written

$$(2.22) \quad \phi(r, z, t) = \sqrt{2/r} \frac{1}{\pi} [1/\sqrt{\epsilon} * J(t)]$$

where

$$\begin{aligned} t &= pr + n_1(z+n) , \quad n_1 = \left(\frac{1}{a_1^2} - p^2 \right)^{1/2} \\ J(t) &= \text{Im} \left(\frac{\sqrt{p}}{n_1} R(p) \frac{dp}{dt} \right) \end{aligned}$$

$$R(p) = (\rho_2 n_1 - \rho_1 n_2) / (\rho_2 n_1 + \rho_1 n_2)$$

and (dp/dt) is the derivative along the Γ contour, namely

$$\begin{aligned} \frac{dp}{dt} &= \frac{n_1 / (R^2/a_1^2 - t^2)^{1/2}}{t < R/a_1} \\ &\quad \frac{i n_1 / (t^2 - R^2/a_1^2)^{1/2}}{t > R/a_1} \end{aligned}$$

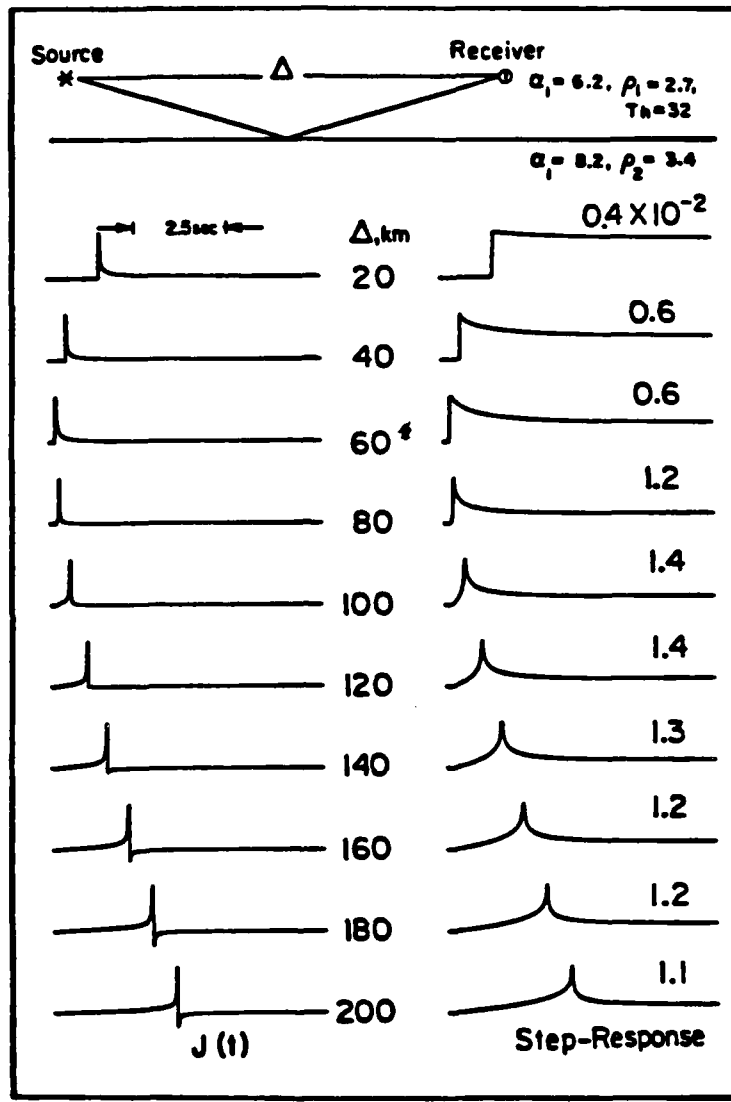


Fig 2.3 - The responses of $J(t)$ and $\phi(t)$ as a function of source-receiver separation. Note that the graphical convolution operator at the larger ranges has two parts: before $t = R/\alpha_1$, the square-root singularities are congruent and produce a log similarity at $t = R/\alpha_1$; the second part corresponds to a weighted step response as in figure 2.2.

where $R = ((z + h)^2 + r^2)^{1/2}$ which corresponds to the distance traveled along a Snell's law reflected path.

If $a_2 > a_1$, there will be a critical angle and a head wave. In this case $J(t)$ will start before $t = R/a$, since n_2 becomes complex at $p = 1/a_2$ and $t_c(p = 1/a_2)$ becomes

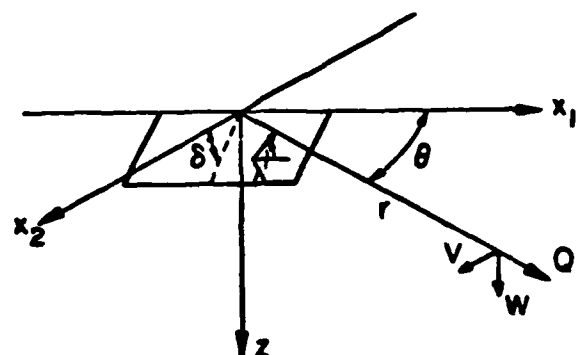
$$t_c = \frac{\pi}{a_2} + \left(\frac{1}{a_1^2} - \frac{1}{a_2^2} \right)^{1/2} (z + h).$$

Evaluating (2.22) numerically, we obtain the step responses displayed in Figure 2.3. Physically, this technique computes the response by summing over all possible ray parameters (p) that interact with the boundary.

b) Shear dislocation (double-couple) source

In this section we will examine some relatively simple dislocation models. Starting with Haskell's representation for shear faulting it is relatively easy to devise the displacements for double couples in an infinite medium, see Harkrider (1976). The solution for a strike-slip fault becomes

Fig 2.4 - Coordinate system for the dislocation formulation where (θ) indicates the strike, (δ) the dip of the hanging wall, and (λ) the motion of the hanging wall relative to the footwall.



$$\begin{aligned}
 \bar{W}(r, z, \omega) &= K \left[\frac{\partial}{\partial z} \left(\frac{\partial^2 A}{\partial r^2} - \frac{1}{r} \frac{\partial A}{\partial r} \right) \right] \sin 2\theta \\
 (2.23) \quad \bar{V}(r, z, \omega) &= K \left[\frac{2}{r} \left(\frac{\partial^2 A}{\partial r^2} - \frac{1}{r} \frac{\partial A}{\partial r} \right) + k_B^2 \frac{\partial B}{\partial r} \right] \cos 2\theta \\
 \bar{Q}(r, z, \omega) &= K \left[\frac{\partial}{\partial r} \left(\frac{\partial^2 A}{\partial r^2} - \frac{1}{r} \frac{\partial A}{\partial r} \right) + k_B^2 \frac{\partial B}{\partial r} \right] \sin 2\theta
 \end{aligned}$$

where W, V and Q are the displacements in the vertical, azimuthal and radial coordinates. The parameters are

$$A = \frac{e^{-\frac{B}{B} R}}{R} - \frac{e^{-\frac{B}{a} R}}{R}$$

$$B = e^{-\frac{B}{B} R}$$

where R = distance between the source and receiver; a, B = compressional and shear velocities, and K = source strength. The spatial derivatives are introduced because of the double-couple nature of the source, and the A and B are simple point source representations as before. Using the Sommerfeld integral, (2.7), and performing the appropriate algebra (see Helmberger 1974) we can express the displacements along the vertical, tangential, and radial coordinates as:

$$\begin{aligned}
 \hat{W} &= \frac{\partial \hat{\phi}}{\partial z} + \omega p \hat{\Omega} \\
 (2.24) \quad \hat{V} &= \frac{1}{r} \frac{\partial \hat{\phi}}{\partial \theta} - \frac{1}{sp r} \frac{\partial^2 \hat{\Omega}}{\partial z \partial \theta} - \frac{\partial \hat{x}}{\partial r} \\
 \hat{Q} &= \frac{\partial \hat{\phi}}{\partial r} - \frac{1}{sp} \frac{\partial^2 \hat{\Omega}}{\partial r \partial z} + \frac{1}{r} \frac{\partial \hat{x}}{\partial \theta}
 \end{aligned}$$

where z , r and θ are the vertical, radial, polar angle coordinates respectively. The P wave potential (ϕ), the SV wave potential (Ω), and the SH wave potential (χ) are expressed by:

P-wave:

$$\begin{aligned}\hat{\phi} = & + \frac{\mu_0}{4\pi\rho} \frac{2}{\pi} \operatorname{Im} \int_c^{+i\rightarrow c} C_1(p) \frac{p}{\eta_\alpha} \exp(-s\eta_\alpha|z-h|) K_2(spr) dp \cdot A_1(\theta, \lambda, \delta) \\ & + \frac{\mu_0}{4\pi\rho} \frac{2}{\pi} \operatorname{Im} \int_c^{+i\rightarrow c} C_2(p) \frac{p}{\eta_\alpha} \exp(-s\eta_\alpha|z-h|) K_1(spr) dp \cdot A_2(\theta, \lambda, \delta) \\ & + \frac{\mu_0}{4\pi\rho} \frac{2}{\pi} \operatorname{Im} \int_c^{+i\rightarrow c} C_3(p) \frac{p}{\eta_\alpha} \exp(-s\eta_\alpha|z-h|) K_0(spr) dp \cdot A_3(\theta, \lambda, \delta)\end{aligned}$$

SV-waves:

$$\begin{aligned}\hat{\Omega} = & + \frac{\mu_0}{4\pi\rho} \frac{2}{\pi} \operatorname{Im} \int_c^{+i\rightarrow c} SV_1(p) \frac{p}{\eta_\beta} \exp(-s\eta_\beta|z-h|) K_2(spr) dp \cdot A_1(\theta, \lambda, \delta) \\ & + \frac{\mu_0}{4\pi\rho} \frac{2}{\pi} \operatorname{Im} \int_c^{+i\rightarrow c} SV_2(p) \frac{p}{\eta_\beta} \exp(-s\eta_\beta|z-h|) K_1(spr) dp \cdot A_2 \\ & + \frac{\mu_0}{4\pi\rho} \frac{2}{\pi} \operatorname{Im} \int_c^{+i\rightarrow c} SV_3(p) \frac{p}{\eta_\beta} \exp(-s\eta_\beta|z-h|) K_0(spr) dp \cdot A_3\end{aligned}$$

SH-waves:

$$\begin{aligned}\hat{\chi} = & + \frac{\mu_0}{4\pi\rho} \frac{2}{\pi} \operatorname{Im} \int_c^{+i\rightarrow c} SH_1(p) \frac{p}{\eta_\beta} \exp(-s\eta_\beta|z-h|) K_2(spr) dp \cdot A_4 \\ & + \frac{\mu_0}{4\pi\rho} \frac{2}{\pi} \operatorname{Im} \int_c^{+i\rightarrow c} SH_2(p) \frac{p}{\eta_\beta} \exp(-s\eta_\beta|z-h|) K_1(spr) dp \cdot A_5\end{aligned}$$

(2.25)

where

s = Laplace transform variable

p = ray parameter

$$\eta_v = (1/v^2 - p^2)^{1/2}$$

h = depth of source

a = compressional velocity

s = shear velocity

ρ = density

M_0 = seismic moment

with the orientation constants given by:

$$A_1(\theta, \lambda, \delta) = \sin 2\theta \cos \lambda \sin \delta + 1/2 \cos 2\theta \sin \lambda \sin 2\delta$$

$$A_2(\theta, \lambda, \delta) = \cos \theta \cos \lambda \cos \delta - \sin \theta \sin \lambda \cos 2\delta$$

$$A_3(\theta, \lambda, \delta) = 1/2 \sin \lambda \sin 2\delta$$

$$A_4(\theta, \lambda, \delta) = \cos 2\theta \cos \lambda \sin \delta - 1/2 \sin 2\theta \sin \lambda \sin 2\delta$$

$$A_5(\theta, \lambda, \delta) = -\sin \theta \cos \lambda \cos \delta - \cos \theta \sin \lambda \cos 2\delta$$

(2.26)

where

θ = strike from the end of the fault plane

λ = rake angle

δ = dip angle

The vertical radiation patterns, as will become apparent shortly, are defined by

$$(2.27) \quad \begin{aligned} C_1 &= -p^2 & SV_1 &= -\epsilon p n_B & SH_1 &= \frac{1}{B^2} \\ C_2 &= 2\epsilon p n_A & SV_2 &= (n_B^2 - p^2) & SH_2 &= \frac{\epsilon}{B^2} \frac{n_B}{p} \\ C_3 &= (p^2 - 2n_A^2) & SV_3 &= 3\epsilon p n_B \end{aligned}$$

where $\epsilon = \begin{cases} +1 & z > h \\ -1 & z < h \end{cases}$

The displacement field for any orientation of a double couple, see Figure 2.4, is the sum of displacement fields of three particular orientations of the double couple, corresponding to the strike-slip fault ($\lambda = 0$ or 180° , $\delta = 90^\circ$), normal dip-slip fault ($90^\circ, 90^\circ$), and the dip-slip fault with a 45° dip ($45^\circ, 90^\circ$), see Burridge et al., (1964).

The index (n) in the expression (2.27) corresponds to (1) strike-slip, (2) dip-slip, and (3) 45° dip-slip.

The integrals expressed in (2.25) can be transformed back into the time domain by the application of the Cagniard-de Hoop technique, see Gilbert and Helmberger (1972) and Harkrider and Helmberger (1977). For example, the field function defined by

$$(2.28) \quad \bar{\xi}_n(\tau, z, s) = \frac{2}{\pi} s \operatorname{Im} \int_c^{i=\infty} \frac{p}{n_v} K_n(spr) e^{-sn_v|z-h|} dp$$

becomes

(2.29)

$$\xi_n(\tau, z, t) = \frac{2}{\pi} \frac{\partial}{\partial \tau} \operatorname{Im} \int_0^t \frac{c_n(\tau, \tau)}{(t-\tau)^{1/2} (t-\tau+2pr)^{1/2}} \left(\frac{dp}{d\tau} \right) \frac{p(\tau)}{n_v} d\tau,$$

where

$$c_n(t, \tau(p)) = \cosh \left(n \cosh^{-1} \left(\frac{t-\tau+pr}{pr} \right) \right)$$

The geometry is given in Figure 2.1a and the de Hoop contour in Figure 2.1b, see de Hoop (1960). The various functions of p are to be evaluated along Γ defined by choosing those values of p which make (t) real and increasing where

$$\tau(p) = pr + n_v |z-h|.$$

The transformation of "p" to "τ" follows from the algebra discussed in the last section.

In this simple case we have a closed form solution for various values of n since the equivalent form back in the (ω, k) domain has been evaluated by Harkrider (1976). For example,

$$\epsilon_2(\tau, z, t) = \frac{\partial}{dt} \left\{ \left[\frac{1}{R} + \frac{2V}{z^2} \left(t - \frac{R}{V} \right) \right] B \left(t - \frac{R}{V} \right) \right\}$$

where the near-field contribution appears in terms of r . However, since we need to evaluate integrals similar to (2.25) with complicated complex integrands later it should be noted that (2.29) can be evaluated for various values of (t) after a change of variable as discussed earlier. A relatively fast evaluation of this type of integral is by nonuniform quadrature techniques where the point spacing is determined by the rate of change of the integrand. The accuracy of such techniques are discussed in Helmberger and Harkrider (1978). We will examine some

useful approximations by expanding the integrand of (2.29) in terms of $(t - \tau)^{-\frac{1}{2}}$. Note that

$$c_n(t, \tau, p) = \frac{1}{2} \left[\frac{(y + (y^2 - 1)^{1/2})^{2n} + 1}{(y + (y^2 - 1)^{1/2})^n} \right]$$

where

$$y = (t - \tau + pr)/pr$$

and

$$\frac{c_n(t, \tau, p)}{(t - \tau + 2pr)^{1/2}} \approx \frac{1}{\sqrt{2pr}}$$

to first order. Thus, we can approximate (2.29) by

$$\begin{aligned} \zeta_n(v, z, t) &= \frac{2}{\pi} \frac{\partial}{\partial t} \operatorname{Im} \int_0^t \frac{1}{\sqrt{2pr}} \frac{1}{(t-\tau)^{1/2}} \frac{dp}{d\tau} \frac{p}{\eta_v} d\tau \\ (2.30) \quad &= \frac{d}{dt} \left[\frac{1}{\sqrt{t}} * \operatorname{Im} \left(\sqrt{2/\pi} \frac{1}{\pi} \frac{\sqrt{p}}{\eta_v} \frac{dp}{dt} \right) \right] \end{aligned}$$

This expression was obtained earlier by using the first term of the asymptotic form of the modified Bessel function. With this degree of accuracy, called the high-frequency solution, the expressions (2.25) can be greatly simplified. We obtain

$$\begin{aligned} \hat{\phi} &= \frac{M_0}{4\pi p} \sum_{j=1}^3 A_j(\theta, \lambda, \delta) \frac{2}{\pi} \operatorname{Im} \int_0^{+1-i\infty} c_j \frac{p}{\eta_\alpha} \sqrt{(\pi/2spr)} \times [\exp(-s(pr+\eta_\alpha|z-h|)) dp] \\ \hat{\omega} &= \frac{M_0}{4\pi p} \sum_{j=1}^3 A_j(\theta, \lambda, \delta) \frac{2}{\pi} \operatorname{Im} \int_0^{+1-i\infty} s v_j \frac{p}{\eta_\beta} \sqrt{(\pi/2spr)} \times [\exp(-s(pr+\eta_\beta|z-h|)) dp] \\ \hat{x} &= \frac{M_0}{4\pi p} \sum_{j=1}^2 A_{(j+3)}(\theta, \lambda, \delta) \frac{2}{\pi} \operatorname{Im} \int_0^{+1-i\infty} s H_j \frac{p}{\eta_\beta} \sqrt{(\pi/2spr)} \times [\exp(-s(pr+\eta_\beta|z-h|)) dp] \end{aligned} \quad (2.31)$$

where we are essentially assuming that the source duration, T , is

$$T \ll 2p_r.$$

We still further approximate (2.30) by assuming

$$\frac{dp}{dt} = \frac{4\pi V}{(t-t_R)^{\frac{1}{2}}(2t_R)^{\frac{1}{2}}}$$

where $t_R = R/V$ and $p = p_0$ and (2.30) reduces to

$$\zeta_n(r, z, t) = \delta(t-t_R)/R$$

called the first motion approximation. This approximation is valid at teleseismic distances where the ratio of travel time to duration is of the order of 100 or greater and has proven quite useful in modeling shallow earthquakes, see Langston and Helmberger (1975).

Transforming the expressions (2.31) into the time domain we obtain:

$$(2.32) \quad \begin{aligned} \phi &= \frac{M_0}{4\pi\rho} \sum_{j=1}^3 A_j(\theta, \lambda, \delta) C_j \frac{H(t - (R/\alpha))}{R} \\ \Omega &= \frac{M_0}{4\pi\rho} \sum_{j=1}^3 A_j(\theta, \lambda, \delta) SV_j \frac{H(t - (R/\beta))}{R} \\ x &= \frac{M_0}{4\pi\rho} \sum_{j=1}^2 A_{j+3}(\theta, \lambda, \delta) SH_j \frac{H(t - (R/\beta))}{R} \end{aligned}$$

Thus, the potentials contain the classical vertical radiation patterns in terms of the $C_j(p)$, $SV_j(p)$, and $SH_j(p)$ and the horizontal pattern in terms of the A_j 's. We will use these expressions in discussing the teleseismic results later.

c) Response of a layer/halfspace: Digression

Using the concepts of generalized ray theory and retaining only the first term of the asymptotic solution, we can construct the (SH) solution on a free surface, namely

$$(2.33) \quad v(r, 0, \theta, t) = \frac{M_0}{4\pi\rho_0} \frac{d}{dt} \left[\dot{D}(t) + \sum_{j=1}^2 A_{j+3}(\theta, \lambda, \delta) v_j(t) \right] ,$$

where

$$v_j(t) = \sqrt{2/r} \frac{1}{\pi} \left[\frac{1}{\sqrt{t}} + \sum_{i=1}^n \text{Im} \left(\frac{\sqrt{p}}{\eta_i} SH_j(p) \Pi(p) p \frac{dp}{dt_i} \right) \right]$$

$D(t)$ = dislocation history

$\dot{D}(t)$ = far-field time function

$\Pi(t)$ = product of the transmission and reflection coefficients

Σ = summation over contributing rays

For the case of a pure strike-slip dislocation embedded in a homogeneous halfspace

$$(2.34) \quad v_j = v_1 = (2 \sin i / \beta^3) H(t - t_R) / R$$

where (i) is the angle of incidence, see Figure (2.1a). Substituting (2.34) into (2.33) we obtain

$$(2.35) \quad v = (M_0 / 4\pi\rho_0) (2F_0 \sin i / \beta^3) \cos 2\theta D(t - t_R) / R$$

where the amplitude is given in centimeters with $F_0 = 10^{-20}$ for unit conversion, and the various parameters expressed as M_0 (ergs), ρ_0 (g/cm³), β (km/sec), R (km) and

$$\gamma = \int_{-\infty}^t \dot{D}(t') dt' = D(-)$$

A factor of 2 has been introduced in the solution (2.35) by the SH free surface receiver coefficient. The far-field step function response for a pure strike-slip event, $v_1(t)$, is given in Figure 2.5, where the model is included as an inset for various values of source depth. The corresponding half-space response is the simple step displayed on each trace. Comparing the response with the source situated just above ($d = 3.5$) and below ($d = 4.5$), one finds that the long-period behavior is nearly the same. The classical type of Love wave dispersion is developed when the layer contains the source and is well understood in terms of ray interference. When the source is located below the layer, the interpretation is more difficult but can be studied by examining the various rays. The ray descriptions become:

$$\begin{aligned}t_1 &= pr + \eta_2(d-h) + \eta_1 h \\t_2 &= pr + \eta_2(d-h) + \eta_1(3h) \\t_n &= pr + \eta_2(d-h) + \eta_1(2n-1)h\end{aligned}$$

$$\begin{aligned}\Pi_1 &= T_{21}(p) \\ \Pi_2 &= T_{21}(p) R_{12}(p) \\ \Pi_n &= T_{21}(p) R_{12}^{n-1}(p)\end{aligned}$$

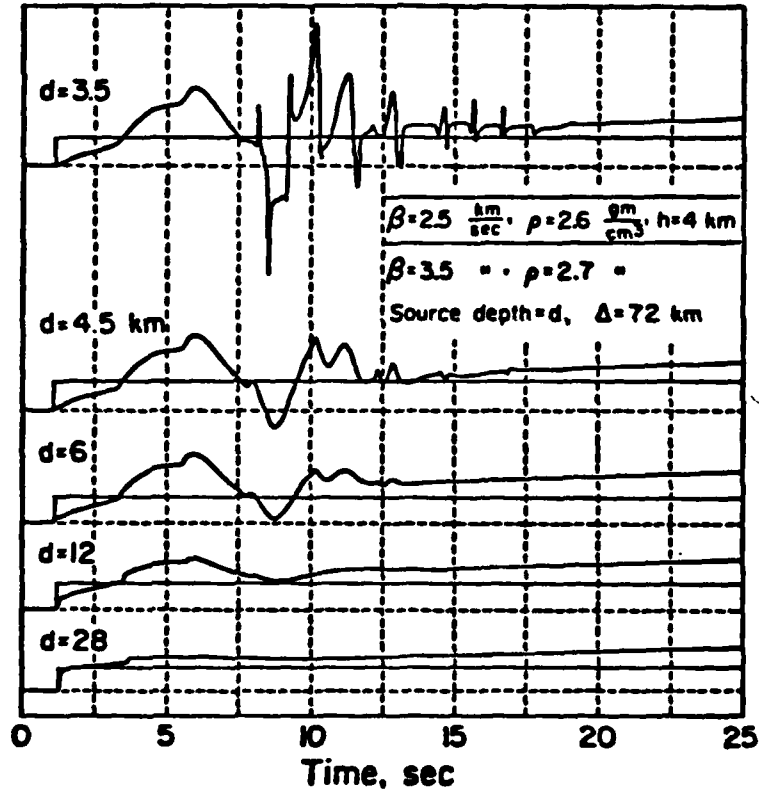


Fig 2.5 - SH step responses at the surface assuming a point strike-slip dislocation situated at various depths. The amplitudes are scaled relative to the top trace with the step response for a homogeneous half-space (bottom properties) displayed for comparison.

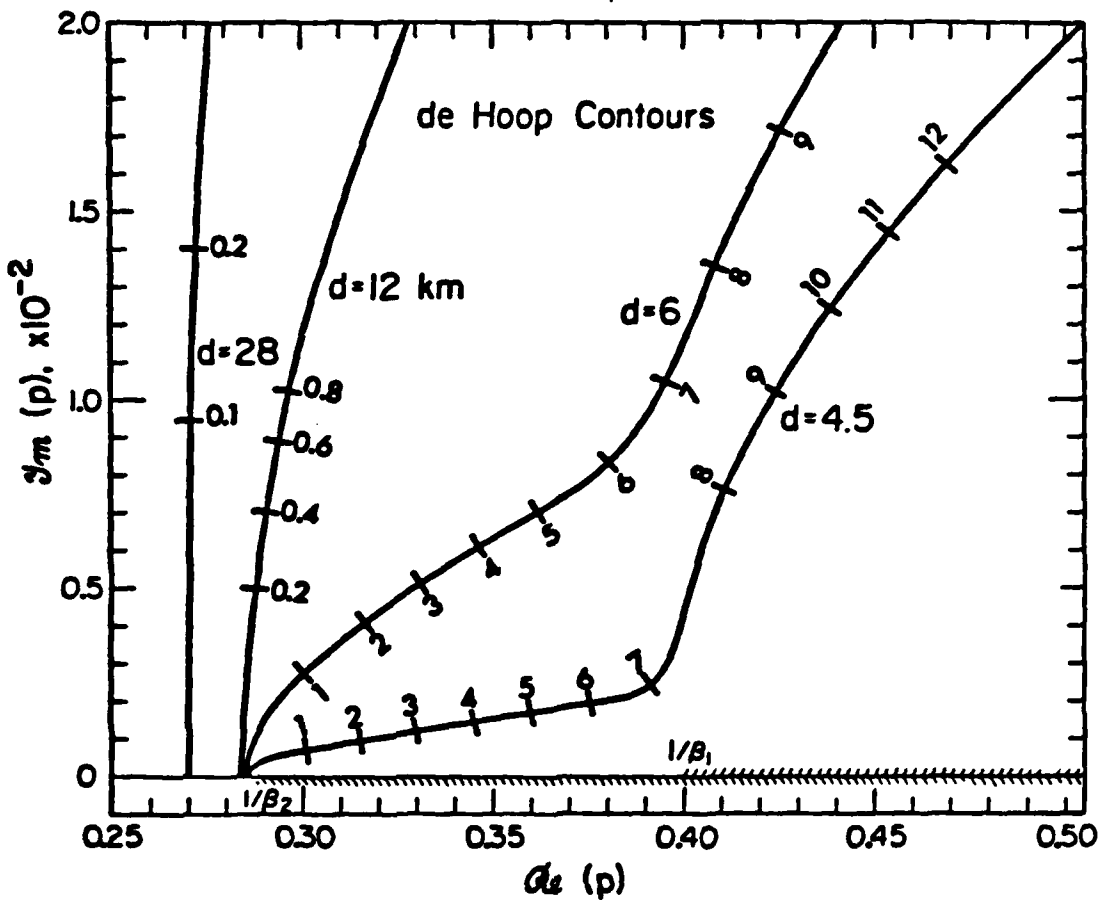


Fig 2.6 - Contours of Im versus $Re(p)$ for the direct rays shown in Figure 2.5. The branch cuts run along the $Re(p)$ coordinate, starting at $1/\beta_2$ and $1/\beta_1$, respectively. The parameter time is marked along each contour.

where the index (1) refers to the layer parameters and (2) to the bottom halfspace.

The coefficients are:

$$R_{12}(p) = (u_1 n_1 - u_2 n_2) / (u_1 n_1 + u_2 n_2)$$

and

$$T_{21}(p) = (2u_2 n_2) / (u_1 n_1 + u_2 n_2)$$

where

$$u_1 = \rho_1 \beta_1^2, \quad u_2 = \rho_2 \beta_2^2$$

Each ray in the solution must be evaluated along its own contour which is determined by inverting these polynomial equations, $p(t_n)$, where t is positive real and increasing from 0 to ∞ . The contours used to compute the direct rays, (t_1) , for the responses in Figure 2.5 are shown in Figure 2.6. The parameter (t) is, also, plotted along these contours and it is easy to see that abrupt increases in $\text{Im}(dp/dt)$ lead to arrivals in Figure 2.5.

Note that $\text{Im}(dp/dt)$ always starts with the square-root singularity. This singularity yields the geometric ray arrival. For large source depths, the contour is near vertical and the synthetic waveform closely resembles the geometric ray response. The first motion approximation is actually equivalent to the saddle point approximation which assumes that the contour goes straight up to (∞) . Thus, the first motion approximation is useful for teleseismic studies. An example application of this technique of earthquake modeling is given in Figure 2.7. The observed displacement is from a simple strike-slip earthquake occurring in the Imperial Valley, California. The only unknown parameters in this particular situation were the depth and slip history, $D(t)$. After a diligent search, the source depth of 7 km and a $D(t)$ specified by triangular pulse with duration 1.5 sec was determined (see Heaton and Helmberger 1978). Similar studies have been conducted by Heaton and Helmberger (1977) and Helmberger and Malone (1975). A rather common observation in modeling multi-bounce phases is that they tend to change their character relatively rapidly. For instance, many times the first few bounces will appear nearly identical at neighboring

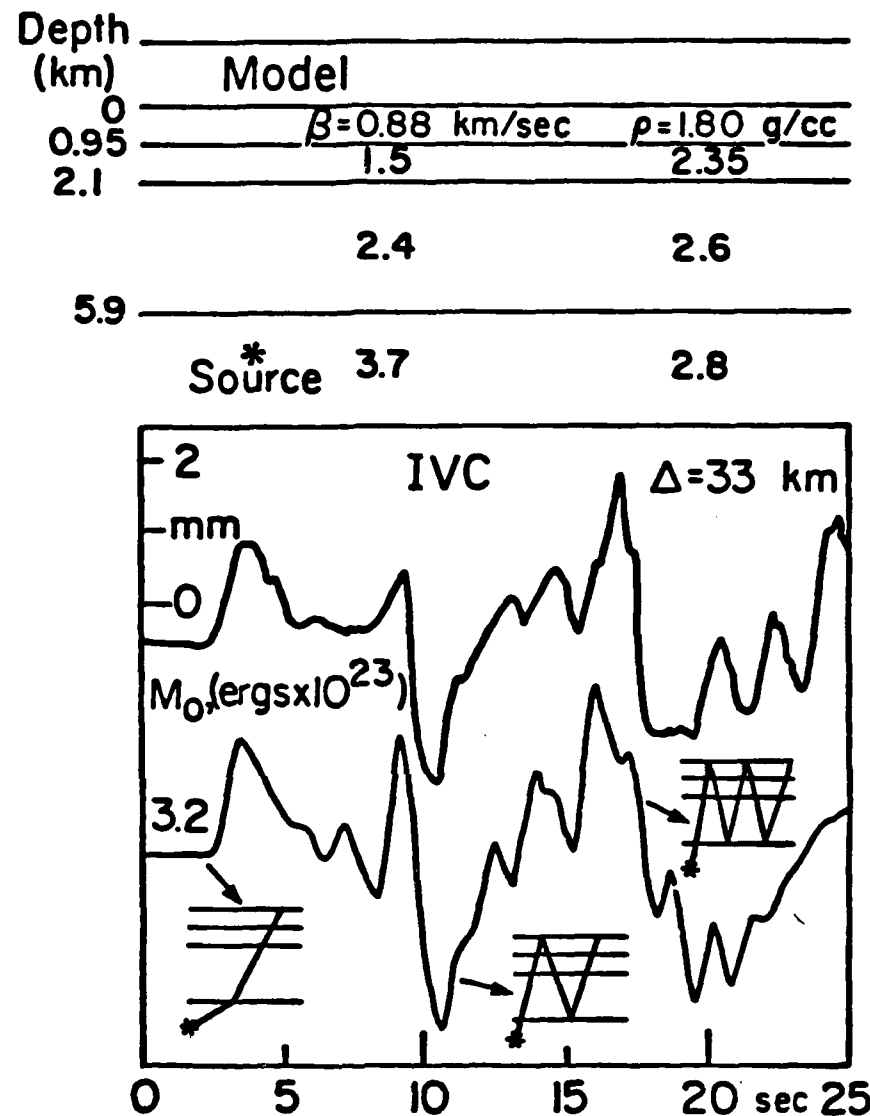


Fig 2.7 - Comparison of a synthetic with a strong motion recording, IVC, of an earthquake occurring at Brawley, California, in November 1976. The model parameters expressing the known structure are given at the top of the figure with the source at a depth of 6.9 km. The three most important rays are indicated schematically.

stations as predicted for flat layers. However, the next bounce will suddenly be missing or too large at these same stations. Another common feature is a sudden change in frequency content of the multiples. Such effects could be caused by lateral variation in the low-velocity waveguide near the surface. A simulation of the effects of a simple dipping interface is displayed in Figure 2.8 (see Hong and Helmberger 1977). In this particular case, the rays can go beyond critical angle after bouncing and thus, produce high frequency reflections. Some progress on treating smoothly varying 3-dimensional structure is presented by Hong and Helmberger (1977).

d) Full Cagniard Solution

The high frequency solutions given by (2.31) have many advantages in model studies as just discussed. However, for small values of (spr), one must use the full solution by applying the transformation given in expression (2.29). The displacements are obtained by substituting expressions (2.25) into (2.24) and performing the Cagniard-de Hoop technique. The results are complicated because of the near-field terms. The tangential motions become:

$$\begin{aligned}
 v(r, z, \theta, t) &= \frac{M_0}{4\pi\rho_0} \frac{d}{dt} [\dot{D}(t) * \sum_{j=1}^2 A_{j+3} v_j] \\
 v_1(r, z, \theta, t) &= \frac{2}{\pi} Im \int^t g_B(2) S H_1 R_T d\tau \\
 &\quad + \frac{2}{\pi} Im \iint^t g_B(2) S H_1 R_T \left(\frac{2}{pr}\right) d\tau dt \\
 &\quad + \frac{2}{\pi} Im \iint^t g_a(2) C_1 R_{PT} \left(\frac{2}{r}\right) d\tau dt \\
 &\quad + \frac{2}{\pi} Im \iint^t g_B(2) S V_1 R_{ST} \left(\frac{2}{r}\right) d\tau dt
 \end{aligned}$$

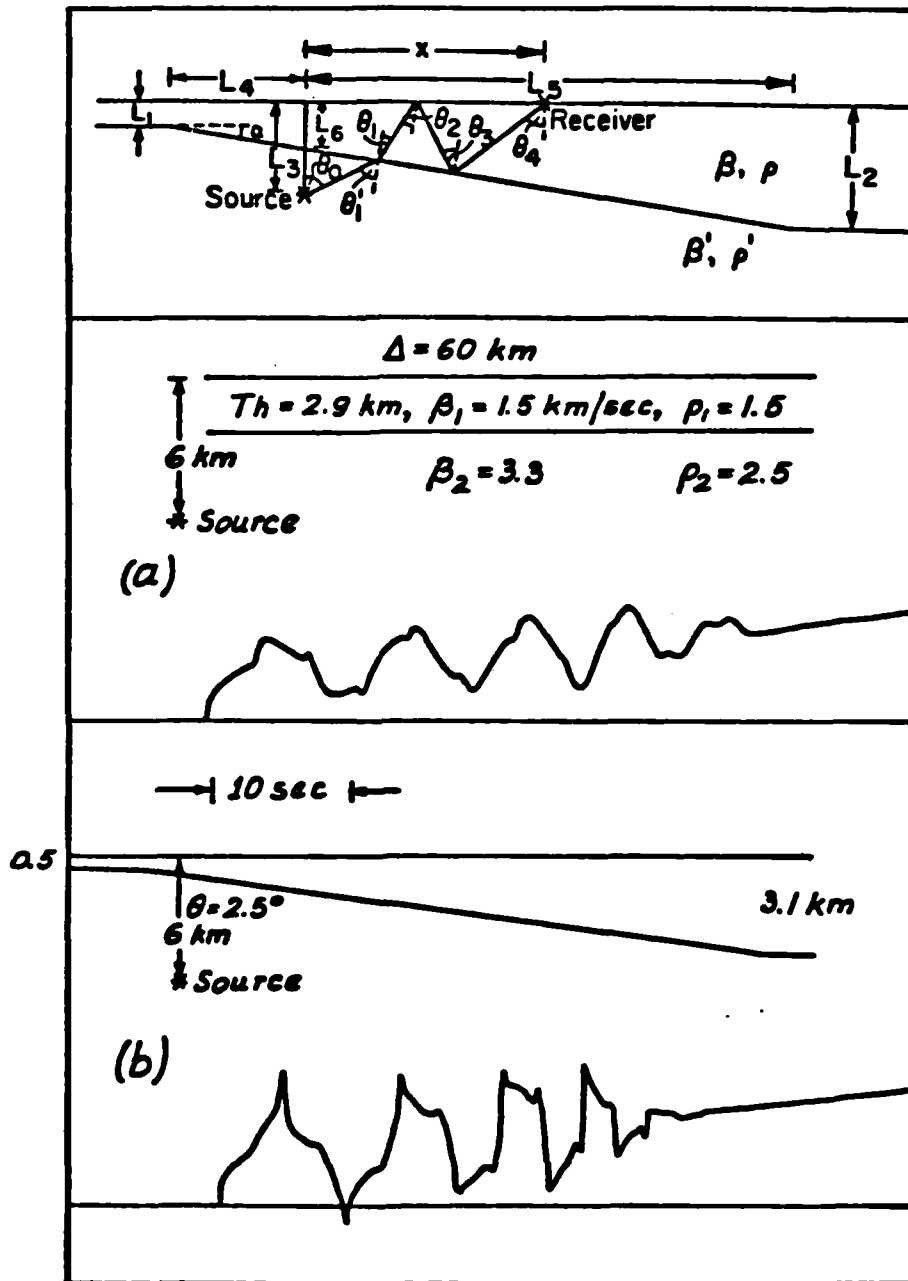


Fig 2.8 - Comparison of the step responses for a flat and dipping layer where the elastic parameters are the same.

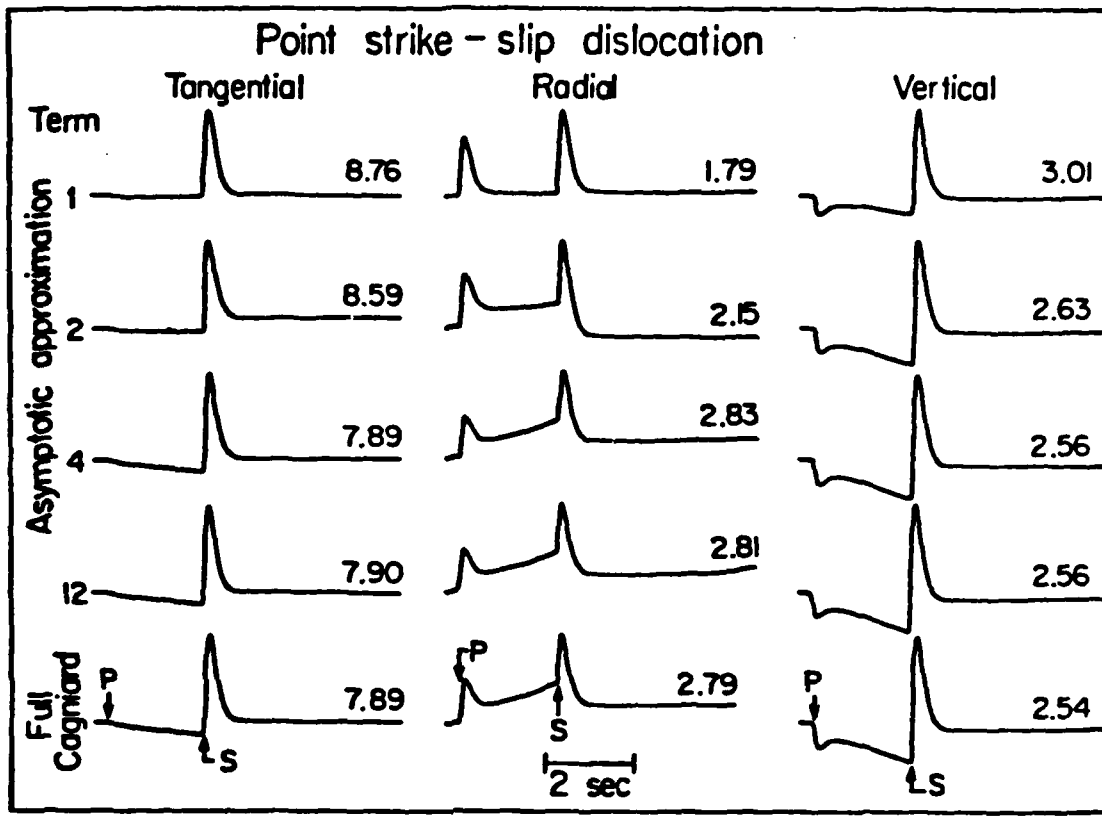


Fig 2.9 - Comparison of the various components of motion for a strike-slip orientation at $\Delta = 16$ km for a whole space. The top four rows contain the asymptotic summation after 1, 2, 4, and 12 items. The full solution is displayed on the bottom.

where

$$R_T = p, \quad R_{PT} = 1, \quad R_{ST} = -\eta_B/p \quad \text{for whole space}$$

and

$$R_T = 2p, \quad R_{PT} = \frac{4\eta_\alpha\eta_\beta}{\beta^2 R(p)}, \quad R_{ST} = \frac{-2\eta_B}{p} \frac{(\eta_B^2 - p^2)}{\beta^2 R(p)}$$

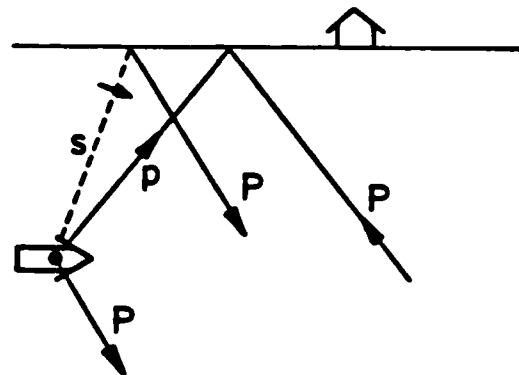
for a receiver on the free surface. The dip-slip result is similar with $n = 1$ and where the factor in parentheses is reduced by two.

An evaluation of this expression for a whole space is given in figure 2.9, where the near-field contributions are apparent. The asymptotic solution is included for comparison. These computations are expensive and their applications to data complicated, see for instance Helmberger and Harkrider (1978) and Heaton and Helmberger (1979). Thus, we will limit our discussion to the more useful approximations where near-field terms can be neglected.

3. Modeling at Teleseismic Distances

Synthetic seismograms can be constructed for comparison with teleseismic observations by putting together the various sub-operations discussed in the previous sections. We will be primarily interested in shallow events where independent information is many times available. Thus, we must correct for the free surface. The simplest correction for this situation is to assume ideal elastic interaction and include the reflected phases, namely pP , and sP (see Figure 3.1). Using the expressions (2.24) and (2.32) and the concepts of GRT (see Appendix A)

Fig 3.1 - Schematic representation of the phases P , pP , and sP .



we can approximate the vertical response at the receiver,

$$(3.1) \quad w = \frac{M_0}{4\pi\rho_0} \sum_{j=1}^3 \left[c_j(p_0) \delta(t) + c_j(p_0) R_{pp}(p_0) \delta(t - \Delta t_1) + sv_j(p_0) \frac{\eta_\alpha}{\eta_\beta} R_{sp}(p_0) \delta(t - \Delta t_2) \right] A_j \frac{R|_{PZ}(p_0)}{R}$$

where

$$\Delta t_1 = 2H\eta_\alpha, \text{ time lag of } pP$$

$$\Delta t_2 = H(\eta_\alpha + \eta_\beta), \text{ time lag of } sP$$

H = source depth

$\delta(t)$ = $\delta(t)$, delta function

The expression in brackets can be represented by three spikes with various strengths, depending on the source orientation, referred to as stick diagrams, see Figure 3.2. The diagram given in the first column displays this information, along with the timing of the three interacting phases, P , pP , and sP , for the three fundamental faults. Crustal layering is easily incorporated by applying ray summations as discussed in the previous section. We assume $t_a^2 = 1$ and that the $(1/R)$ geometric spreading term in the homogeneous case can be replaced by the effective "1/R" from Figure 3.3. The synthetics in Figure 3.2 were produced by performing the various convolutions assuming different source durations.

The waveshapes are seriously distorted by the interferences with each fault orientation having its own characteristics. Thus, we can compare these synthetics with observed waveshapes such as those given in

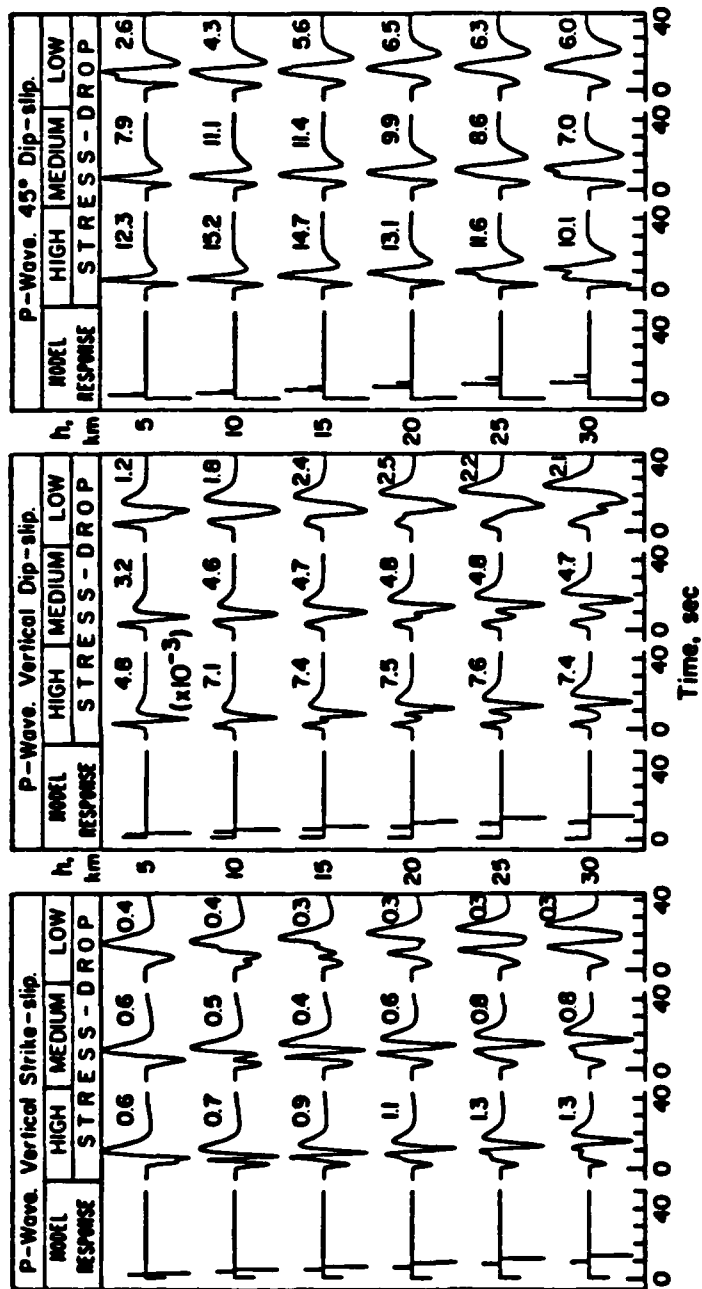


Fig. 3.2 - P-wave synthetic seismograms for the three potential terms with varying depth and time functions. The numbers to the upper right are actual potential amplitudes without the $(M/4\pi p)(1/R)$ and receiver functions included. The source time parameters, δt 's, are high stress-drop (0.5, 1.0, 0.5), medium stress-drop (1.0, 3.0, 1.0), and low stress-drop (2.0, 6.0, 2.0). After Langston and Helmberger (1975).

Figures 3.4, 3.5 and 3.6 to determine the fault parameters; namely, strike, dip, slip vector, fault depth, moment, and δt 's (source time history). Note that for observations near nodes such as BOG and BHP (Figure 3.4) one finds difficulty in determining the polarity of the direct P since it is nearly zero. In cases where $\delta \neq 90^\circ$ we expect sP to still contribute as at BOG since the dip-slip component is strong. Note the strong differences in amplitudes displayed in Figure 3.2 which are caused by the position of the radiation loops.

Considerable ringing occurs for those events situated in some basins and in oceanic environments (see Figure 3.6 and Langston and Blum, 1977, for examples of multi-pathing or situations where many rays are involved in generating the response).

Synthetics for normal and thrust faults are not very interesting since they are nearly identical at all azimuths. As probably suspected,

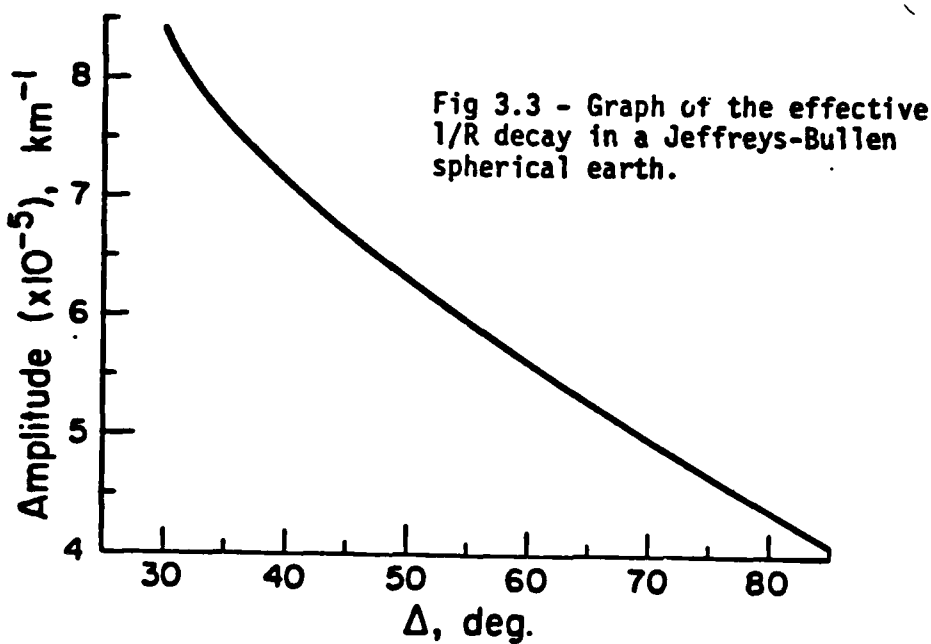


Fig 3.4 - Observed (top) and synthetic (bottom) long period P waveforms at 14 WWSS stations. The P-first motion plot is represented by the equal area stereographic projection of the lower half of the focal sphere. Black dots indicate compression (upward breaking P) and open circles indicate dilatation (downward breaking P). The heavy solid lines denote the nodal planes used in determining the fault orientation, θ (strike), δ (dip), λ (slip direction). Modified after Burdick and Mellman (1976).

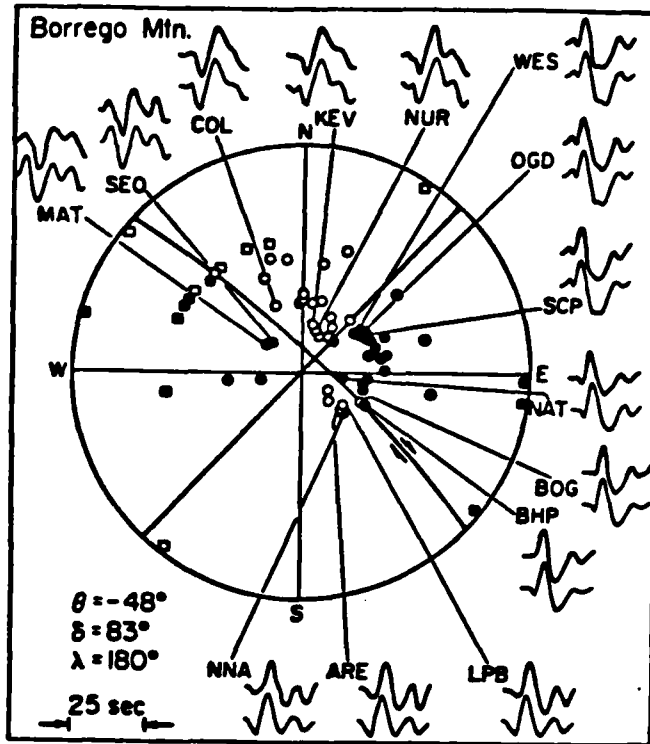
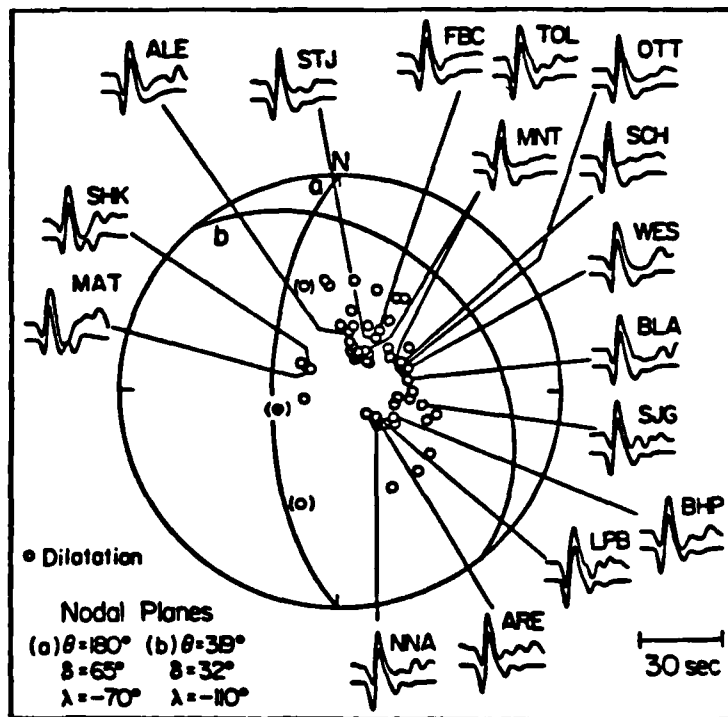


Fig 3.5 - Focal mechanism plot showing the P-first motions for the Oroville earthquake, August 1, 1975. The observed P waveforms are given on the top and synthetic results on the bottom. Modified after Langston and Butler (1976).



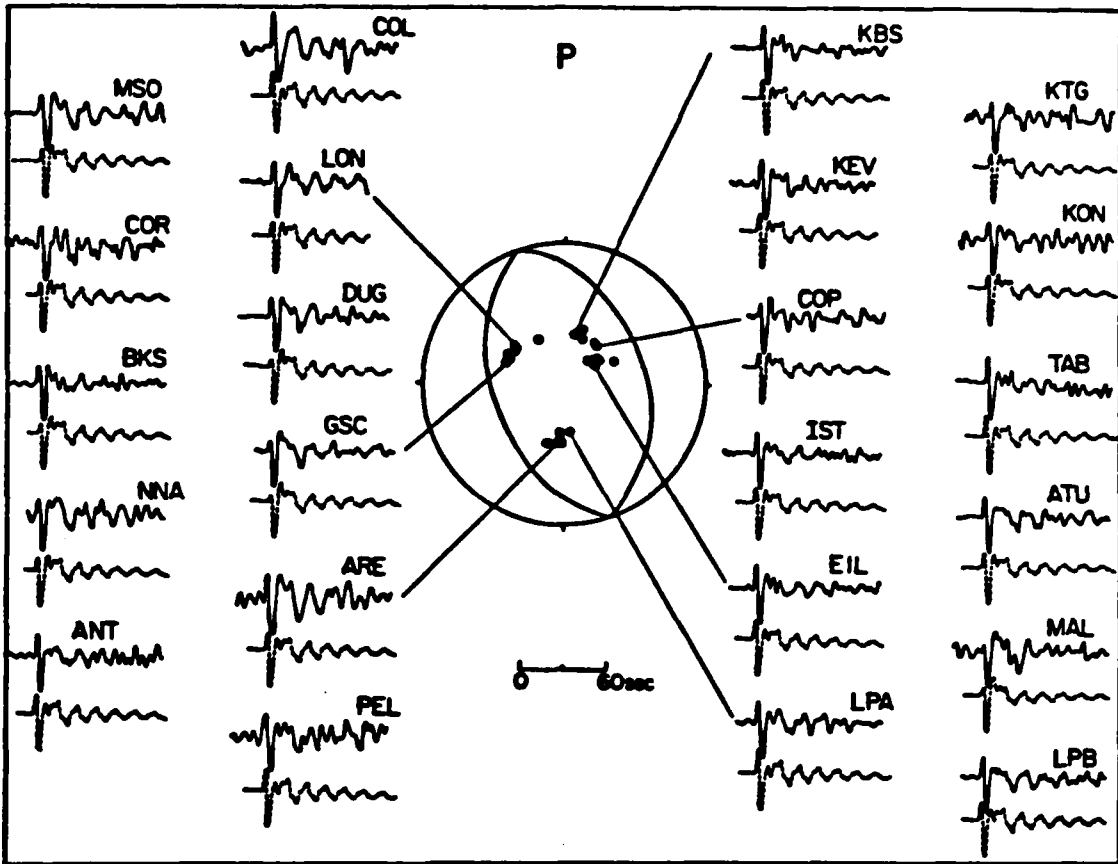


Fig 3.6 - Focal mechanism plot showing the P-first motions for the Bermuda earthquake, March 24, 1978. Observed (upper) and synthetic (lower) P wave traces from the vertical long-period WWSSN seismograms for stations shown in Figure 1. Note an initial simple event followed by more complicated water reverberations (After Stewart and Helmberger, 1981).

this uniformity in waveshape leads to a lack of resolution in fault orientation. We require samples of the energy release at other quadrants, in particular at regional distances. At these distances the earth's mantle structure produces more complicated responses and the $1/R \delta(t-t_R)$ correction is no longer appropriate.

4. Modeling Regional Body-waves

The regional phases can be subdivided into two groups, those less than and those beyond about 12° . At the smaller ranges the response is controlled largely by the crustal waveguide and at larger ranges by the upper-mantle discontinuities, see Helmberger and Engen (1980).

a) Crustal waveguide

We begin by discussing the effects of the crustal waveguide on the P-waves, actually all the energy that travels faster than the S-waves. This portion of the seismogram is commonly referred to as P_n , P_L , and P_{nl} . We assume a point shear dislocation, as before, and that the earth can be treated by a single layer (crust) over a half-space (mantle), see Table 1. Both of these assumptions are obvious oversimplifications but as we will see, worth consideration as viable models at long periods. The vertical displacement, assuming the high-frequency solution, becomes

$$(4.1) \quad w(r, 0, \theta, t) = \frac{M_0}{4\pi\rho_0} \frac{d}{dt} \left[\dot{D}(t) + \sum_{j=1}^3 A_j(\theta, \lambda, \delta) w_j(t) \right]$$

where

$$(4.2) \quad w_j(t) = \sqrt{2/\pi} \frac{1}{\pi} \left[\frac{1}{\sqrt{t}} * \sum_{i=1}^n \text{Im} \left(\frac{\sqrt{p}}{\eta_a} C_j(p) R_{NZ}(p) \pi_i(p) \frac{dp}{dt} \right) \right] \\ + \sqrt{2/\pi} \frac{1}{\pi} \left[\frac{1}{\sqrt{t}} * \sum_{i=1}^n \text{Im} \left(\frac{\sqrt{p}}{\eta_B} S V_j(p) R_{NZ}(p) \pi_i(p) \frac{dp}{dt} \right) \right]$$

where $R_{NZ}(p)$ indicates the appropriate receiver function for either P(N=P) or S(N=S) waves arriving at the station, respectively. The radial displacements, Q_i , are obtained by replacing R_{PZ} and R_{PR} with R_{SZ} and R_{SR} . See Appendix A for definitions of these receiver functions. The summation is over contributing rays where $\pi_i(p)$ defines the product of all the reflection coefficients encountered along the ray path from the source to the receiver, similar to the SH-case considered earlier.

Constructing the solution by summing the rays as described by (4.2) is tedious in that many rays are required to produce reliable synthetics. To ensure stability, ray files containing increasing numbers of multiples are computed sequentially where the output can be monitored per multiple. An example calculation is displayed in Figure 4.1. Since

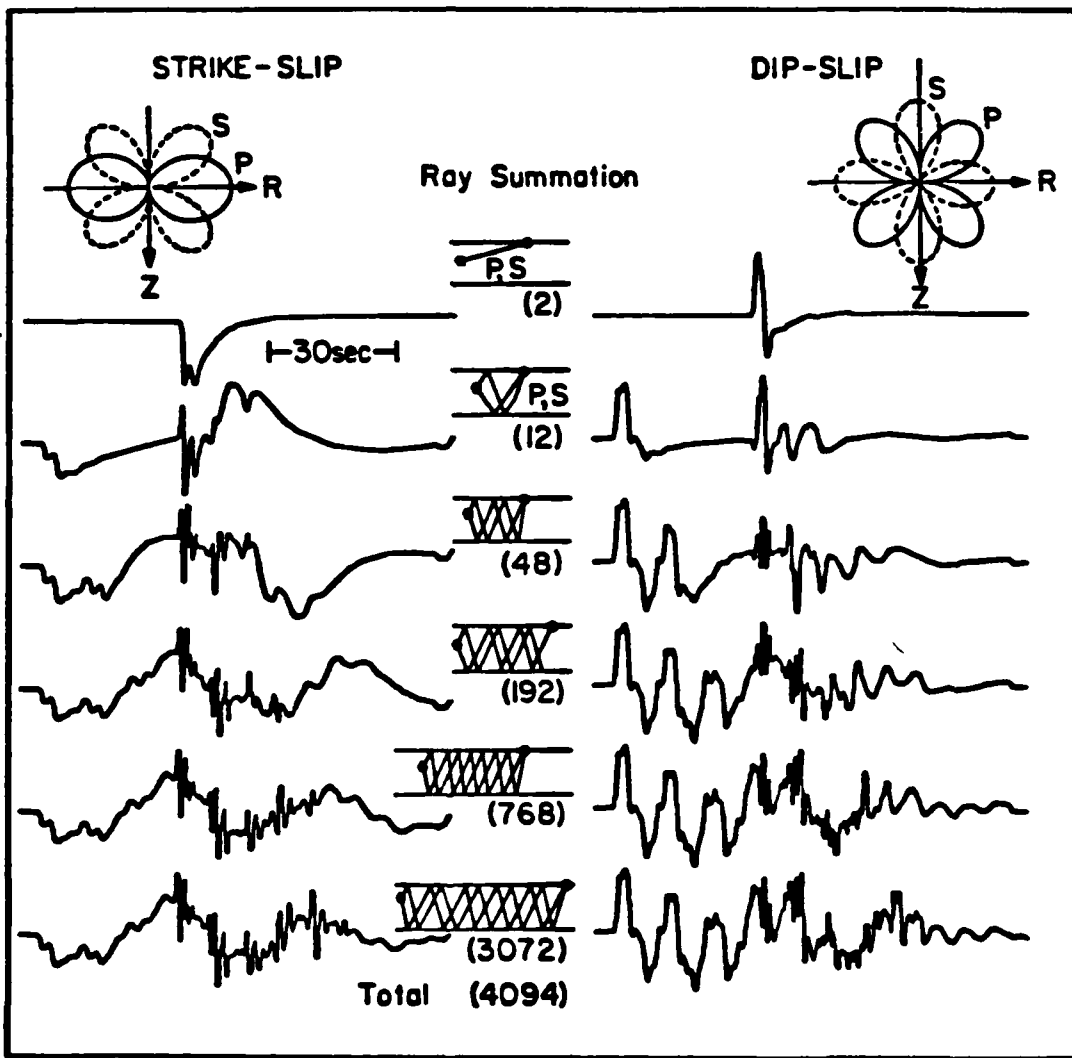


Fig 4.1 - Vertical components of motion as a function of ray summation assuming a trapezoidal time function described by 0.5, 0.5, 0.5, for pure strike-slip and dip-slip orientations at $\Delta = 1000$ km.

the strengths and polarities of the various rays are strongly influenced by the vertical radiation patterns, $C_j(p)$ and $SV_j(p)$, we have included these patterns above each column. Note that due to our limited time window we do not include the direct S pulse. The second pulse arriving in the direct ray response is actually a diffracted arrival, essentially the pulse that travels to the surfaces as an S-wave and along the surface as a P-head wave. The first set of multi-bounce rays produce head waves along the top of the mantle. There are 12 rays in this set, namely

$$2^2 + 2^3 = 12$$

considering the various possible mode changes. The responses in the bottom row were generated by summing all (4,094) rays as a check against a much smaller ray set which takes advantage of the kinematic and dynamic redundancies. For instance, only 304 rays are needed to compute the response for the fifth bounce since most of the rays in the complete set have the same times and amplitudes (see Hron and Kanasewich 1971 or Helmberger 1968 for details).

Another strategy for understanding these motions is to split these ray contributions into those starting upward as opposed to downward (see Figure 4.2). Changing the source depth shifts the upgoing trace relative to the downgoing trace producing a dramatic effect on the dip-slip case as displayed in Figure 4.3. In fact, a good approximate seismogram for $h = 4$ and 16 can be obtained by simply shifting the $h = 8$ traces without recomputing the rays. Partial derivatives with respect

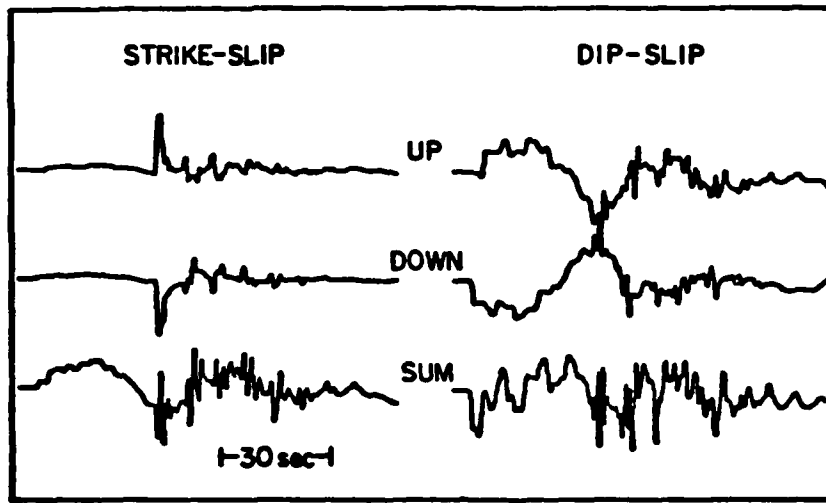


Fig 4.2 - Radial components of motion at $\Delta = 1000$ km in terms of upgoing, downgoing, and summed for trapezoidal time history (0.5, 0.5, 0.5 sec).

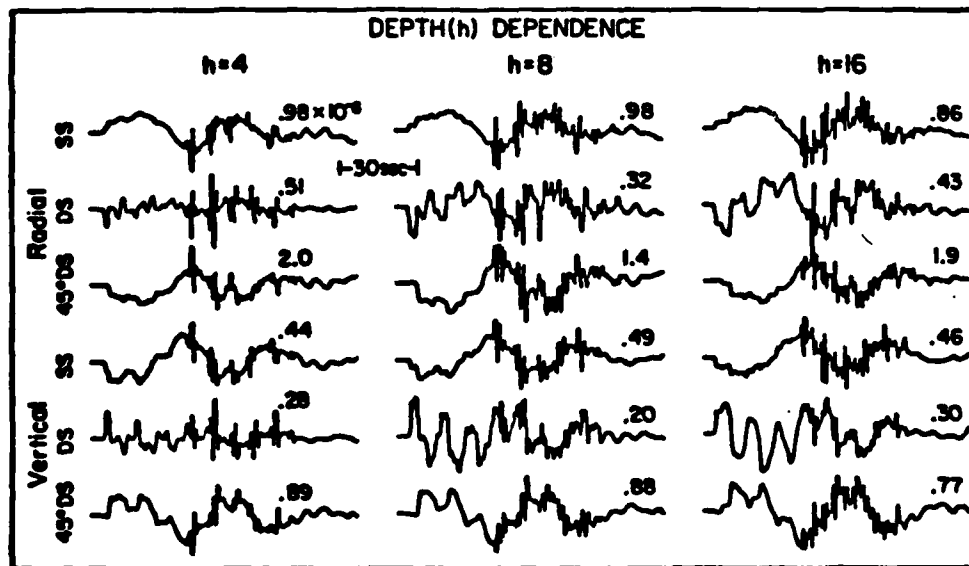


Fig 4.3 - Motions of all three types of faults at $\Delta = 1000$ km as a function of source depth. The numbers above each trace indicate the zero to peak amplitude in centimeters assuming $M_0 = 4\pi\rho_0 \times 10^{20}$ dyne-cm and trapezoidal time history (0.5, 0.5, 0.5 sec).

to changes in velocities or changes in the waveguide can be approximated by stretching or compressing individual ray responses (see Wallace and Helmberger 1982).

For the purpose of studying source mechanisms we can apparently do reasonably well by assuming that common shallow earthquakes occur at a depth of 8 km. Profiles of responses for a dislocation located at this depth are presented in Figure 4.4. Preliminary comparisons of

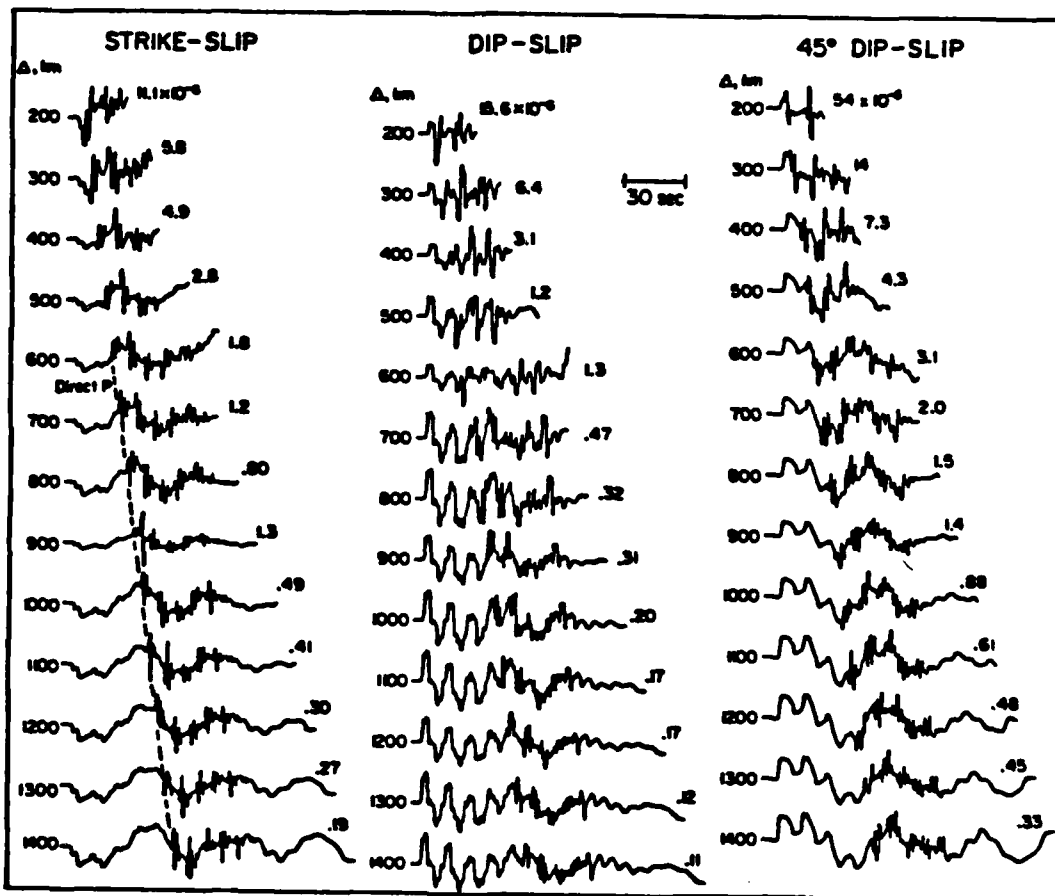
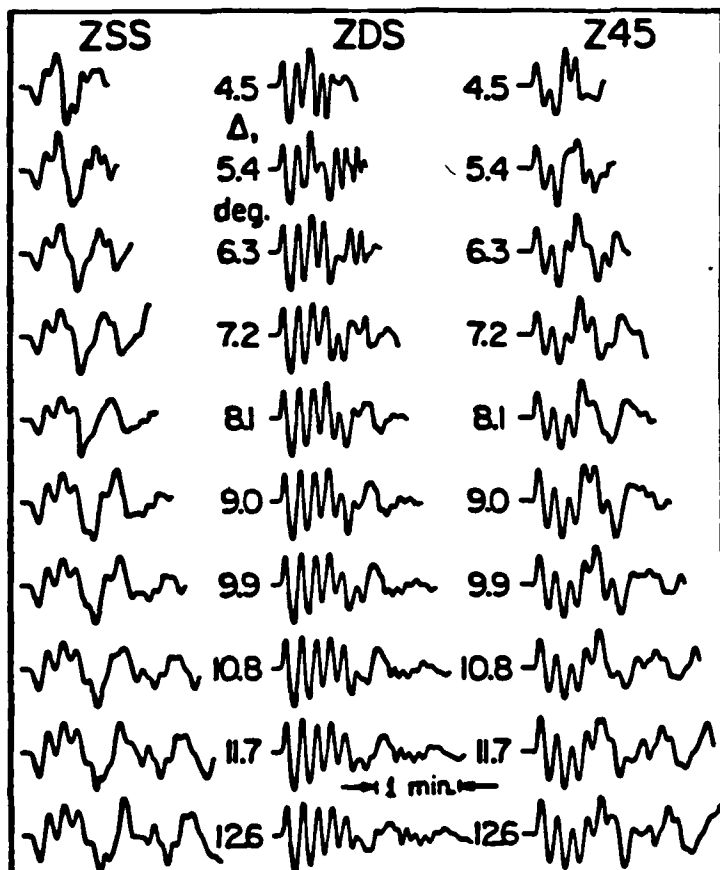


Fig 4.4 - Profiles of the vertical displacements for the three fundamental faults. The numbers above each trace indicate the zero to peak amplitude in centimeters assuming $M_0 = 4\pi\rho_0 \times 10^{20}$ dyne-cm and trapezoidal time history (0.5, 0.5, 0.5 sec). This time history was convolved with the delta function response to reduce the high-frequency spikes created by the post-critical reflections so that the longer periods become more apparent (After Wallace *et al.*, 1981a).

synthetics generated from these responses (see Wallace *et al.*, 1981), indicate that these results are useful on a global scale if the high frequencies are removed. Thus, we will filter these responses and the corresponding observations by convolving with a triangle which has a 2 sec rise and fall. Convoluting these filtered Green's functions with a trapezoid source with 1 sec intervals followed by the long-period WWSSN instrumental response yields the synthetics given in Figure 4.5. This time history is expected for events in the 5 to 6 magnitude class, the size commonly recorded by the network. We propose to model shallow earthquakes at these ranges by simply forming a linear combination of these three fundamental synthetics. The relative strengths of each column is used to fix the fault orientation, namely the strike, dip and slip vector. Some example comparisons of observations and corresponding synthetics are displayed in Figures 4.6, 4.7 and 4.8. These results

Fig 4.5 - Theoretical displacement profiles for the vertical component. The Green's functions were computed from the model presented in Table 1 and have been convolved with a source time function represented by a trapezoid ($t_1=1$, $t_2=1$, $t_3=1$), a triangular filter (2 second rise and fall), and a WWSSN long-period instrument.



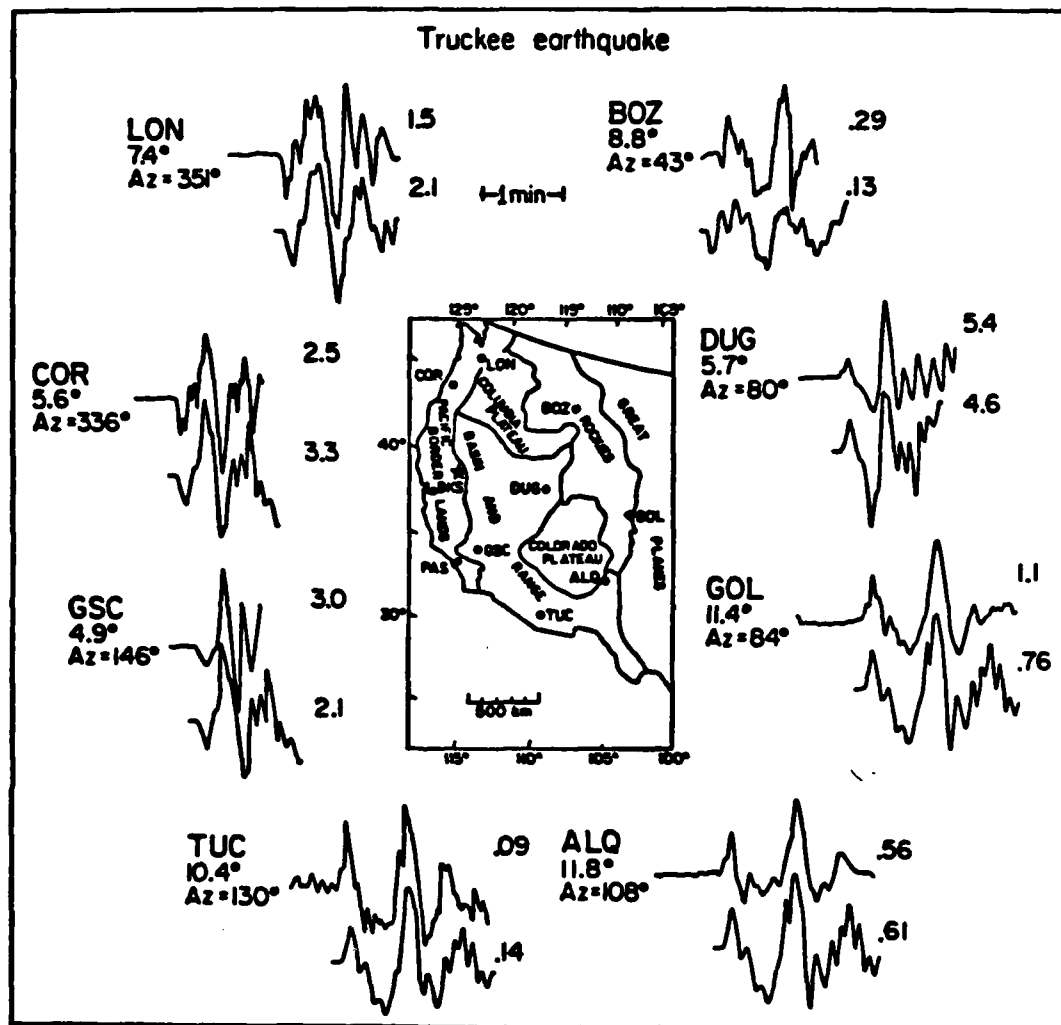


Fig 4.6 - The vertical $P_{n\ell}$ waveforms of the 1966 Truckee earthquake. The star denotes the epicenter. The data is the top trace at each station and the trace below is the synthetic fit. The strike-slip mechanism has two nodal planes which project through TUC and BOZ. To the right of each trace is the observed or predicted amplitude (on the basis of $M_0 = .8 \times 10^{25} \text{ dyne-cm}$) in 10^{-3} cm .

Fig 4.7 - Filtered data and synthetics from the Oroville earthquake. At all the stations except GOL both the vertical (the first trace pair) and radial components are shown.

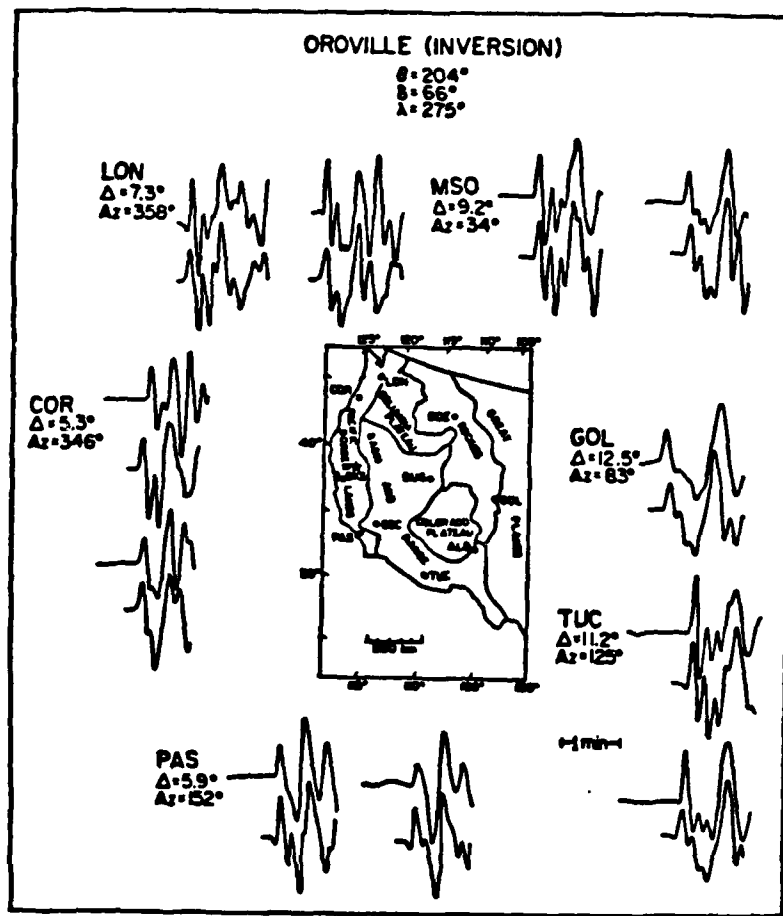
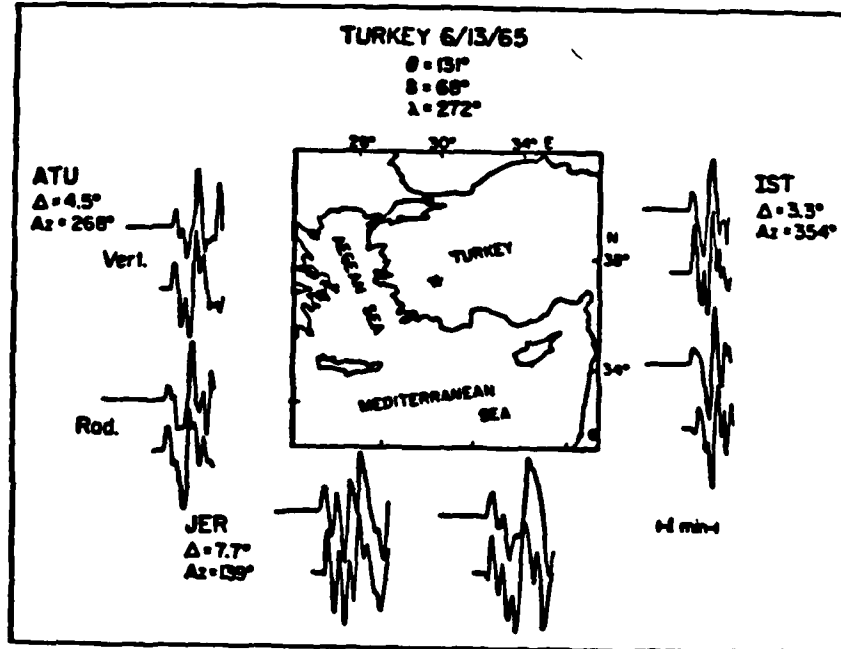


Fig 4.8 - Location of the Turkey event (star) and the recording stations. The filtered data and synthetics for both the vertical and radial components are shown (After Wallace and Helmberger, 1982).



were found by applying a least squares waveform inversion technique. The method involves an iterative scheme which makes use of an error function determined by the cross-correlation of the observed seismogram and a synthetic. Since only three parameters are involved, the scheme proves very effective. The moments are determined by simply comparing the amplitudes of the data with the synthetic and taking the average value. In general, the inversion yields results that are in good agreement with the literature. We will briefly discuss the Truckee event as an example.

The Truckee earthquake was a strike-slip event at 10 km depth which produced excellent regional records but very few teleseismic body wave records as typical of moderate size strike-slip events. The Truckee earthquake ($m_b = 5.7$) has been studied by several authors (Tsai and Aki, 1970, and Burdick, 1977) making it a good test case. Tsai and Aki (1970), from first motion studies and modeling of the surface waves, determined this event to be pure strike-slip on a fault plane striking N44°E and dipping 80°SE. The surface wave moment was determined to be 0.83×10^{25} dyne-cm. Figure 4.6 shows the location of the epicenter, recording stations and filtered data for Truckee. Also shown are the synthetics determined from the inversion results. Note that BOZ and TUC are very nearly nodal. The inversion yields a mechanism which is very similar to Tsai and Aki's (1970); a strike of N43°E, a dip of 76°SE and a rake of -11°. The only significant difference is the slight dip-slip component in our solution, which is also acceptable on the basis of the first motion data. The moment determined from the P_{nl} waveforms is 0.87×10^{25} dyne-cm, which is in agreement with Tsai and Aki (1970).

The results for the Oroville earthquake are particularly interesting in that the observations are nearly all positive as opposed to those observed telesismically, see Figure 3.5. We will discuss this event later after including the waveform observations in the 12° to 30° range.

b) Upper-mantle responses

At distances larger than about 12° the mantle "P" wave begins to emerge. This feature is displayed in Figure 4.9. Near 1000 km the beginning portion of the seismogram is dominated by P_n , that is, a P head wave traveling along the top of the mantle as a head wave. Since this earthquake is nearly a pure strike-slip event we can interpret the first upswing as P_n followed by pP_n and sP_n . Beyond about 12° this combination of arrivals becomes much sharper since they are no longer head waves. Short-period waves from explosions fired at the Nevada Test Site increase in amplitude by nearly two orders of magnitude near this range, for example see Helmberger (1973). These features can be generally explained by the tectonic model presented in Figure 4.10. This smooth model is broken into homogeneous layers suitable for the applications of GRT. Essentially, the generalized rays returning from the interfaces in the mantle are added to the rays discussed earlier (see Figure 4.4). Synthetics appropriate for a strike-slip event are presented in Figure 4.11. The recording at the nearest ranges are essentially the same as displayed in Figure 4.5. The pattern of (P, pP and sP) going from head waves to diving waves is quite apparent. Comparing these results with Figure 4.9 it would appear that the lid

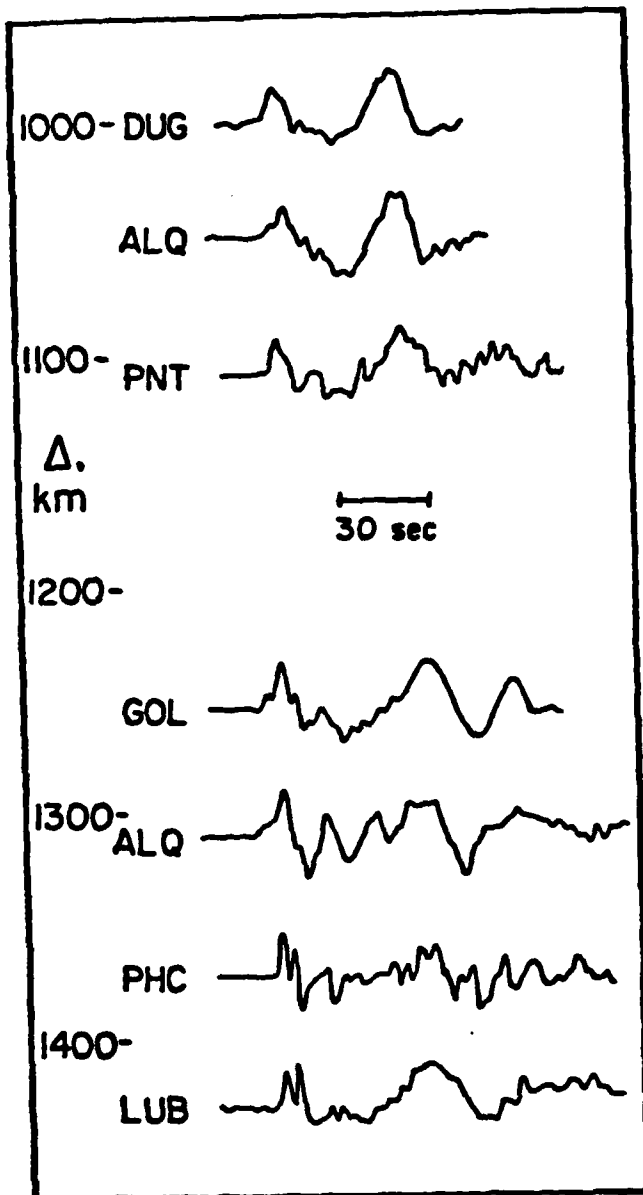


Fig 4.9 - Profile of strike-slip observations from P_{nL} to P. Recordings at DUG, ALQ, and LUB are from the 22 December 1964 event of northern Baja California; the others are of the Truckee event discussed earlier.

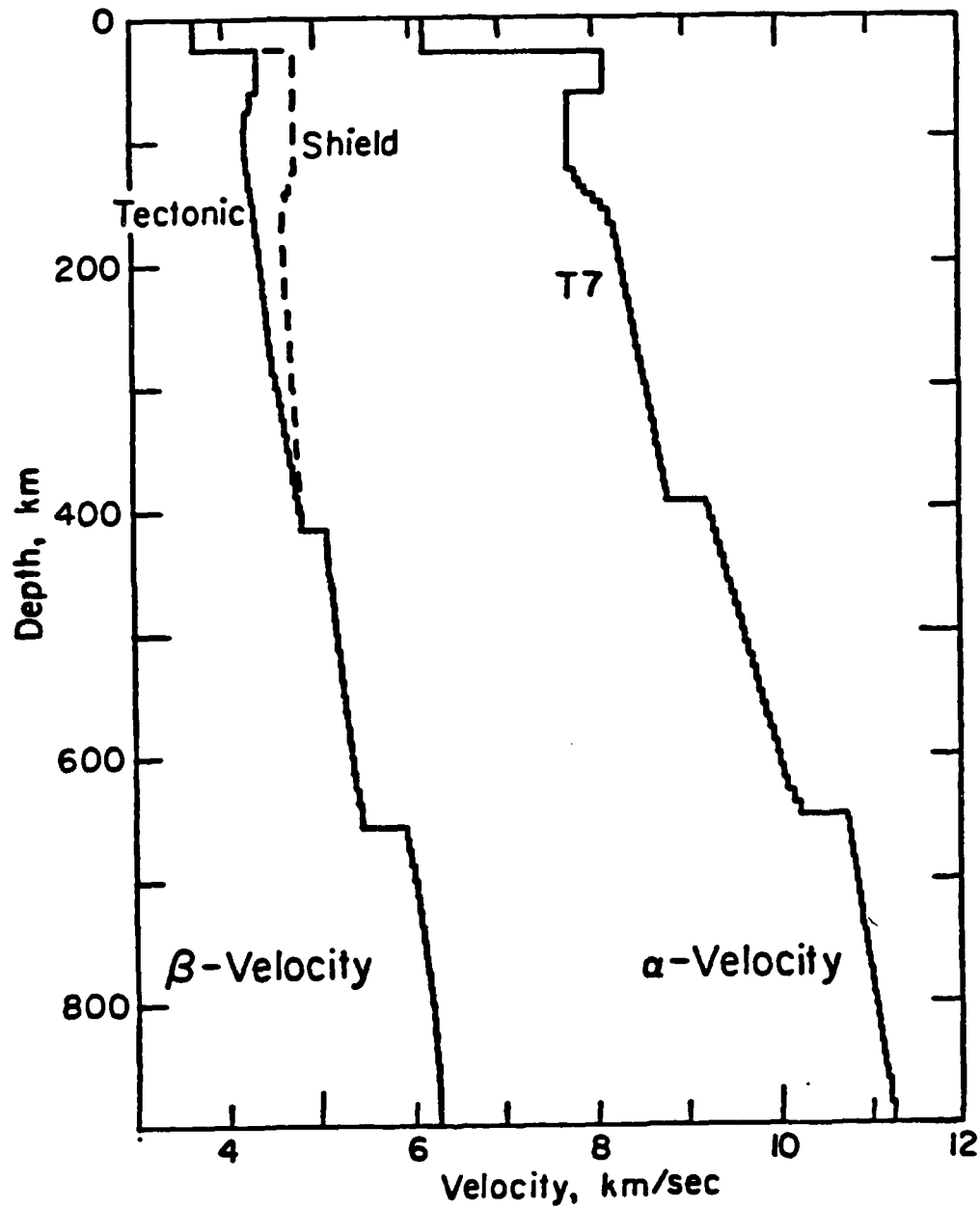


Fig 4.10 - Velocity depth functions for T7
(Burdick and Helmberger, 1978) and two recent
shear-wave models (Grand and Helmberger, 1982).

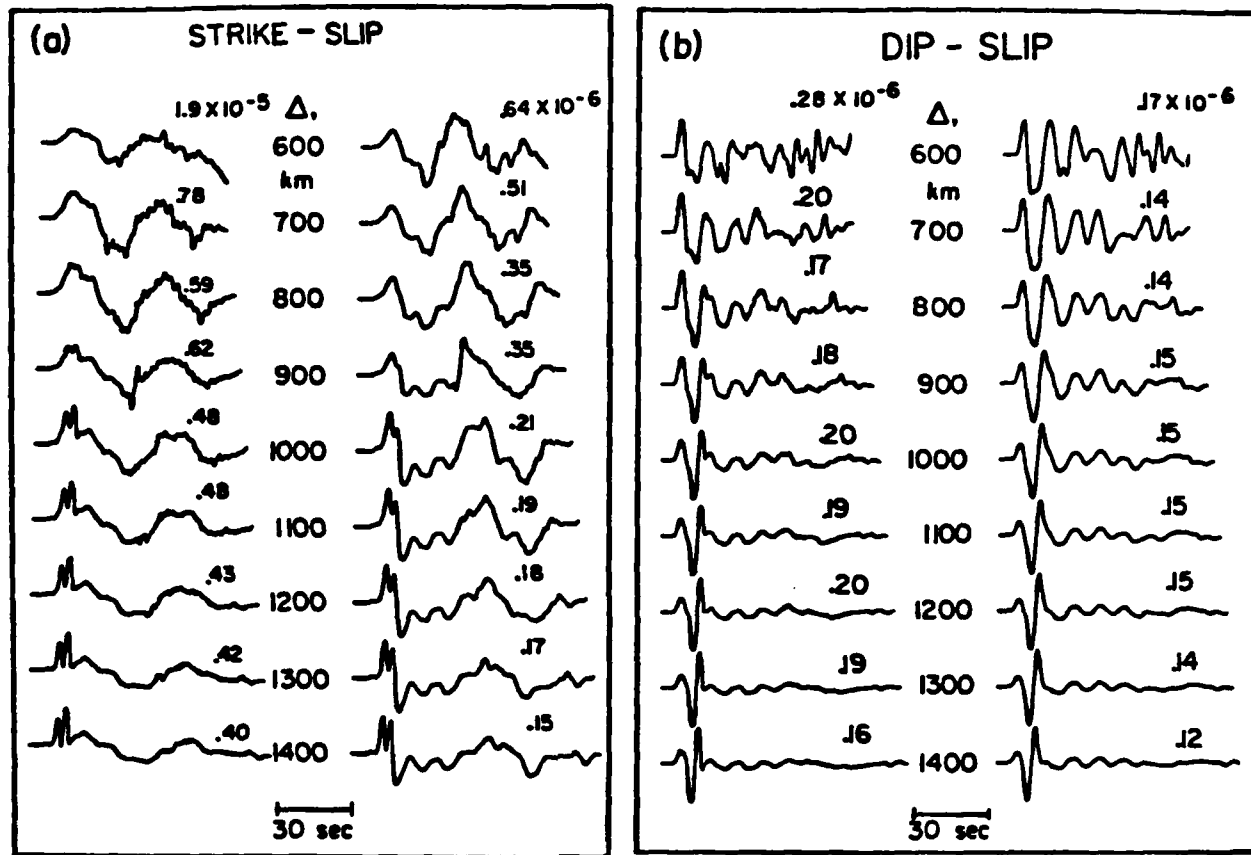


Fig 4.11 - (a) Strike-slip excitation going from $P_{n\ell}$ domination to P and long-period synthetics.
 (b) Dip-slip excitation going from $P_{n\ell}$ domination to P and long-period synthetics.

thickness (the high-velocity layers between the crust and the low-velocity zone) may be too thin in the T7 model. Actually, the crossover distance between P_n to P shows considerable lateral variation. For instance, short-period P_n in shield regions are observed to much larger distances than in other regions. However, since earthquakes rarely occur in shield regions, we will restrict our discussion to model (T7) which appears to be quite useful in simulating earthquake observations in active regions, see for example Burdick (1980).

Nevertheless, we propose omitting records at ranges 12° to 14° as being too regional or structurally dependent to be useful in source modeling in most situations.

The response of the earth models at ranges beyond 15° can be obtained by simply summing primary rays. That is

$$(4.3) \quad M(t) = \sqrt{2/\pi} \frac{1}{\pi} \left(\frac{\Delta}{\sin\Delta} \right)^{1/2} \left[\frac{1}{\sqrt{t}} * J(t) \right]$$

where

$$J(t) = \sum_{j=2}^n I_m \left(\frac{\sqrt{p}}{\eta_j} \left(\frac{dp}{dt} \right)_j I_j(R, T) \right)$$

and

$$I_2 = R_{12}$$

$$I_3 = T_{12} R_{23} T_{21}, \text{ etc.}$$

The term "primary" refers to rays that undergo one reflection only. The $(\Delta/\sin\Delta)$ factor is a correction for spherical spreading, see Gilbert and Helmberger (1972).

Near 30° , $M(t)$ approximates a step with amplitude predicted by the curve in Figure 3.3. Actually, the amplitudes in Figure 3.3 were generated using expression (4.3) assuming the JB model. Similar results are obtained from the geometric formula, Bullen (1965), p. 126:

$$(4.4) \quad A = \left[\frac{1}{r_o^2} \left(\frac{v_o}{r_o} \right) \frac{\tan i_o}{\cos i_o} \left(\frac{1}{\sin\Delta} \right) \frac{d^2 T}{d\Delta^2} \right]^{1/2}$$

where

T is the travel time

Δ is the epicentral distance in degrees

i_0 is the angle of incidence

v_0 is the velocity at the surface

r_0 is the radius of the earth

Because the ray summation has omitted multiples, it appears necessary to document these responses by comparison with other methods. This was done recently by Burdick and Orcutt (1978) with a comparison of GRT and reflectivity results given in Figure 4.12. These same

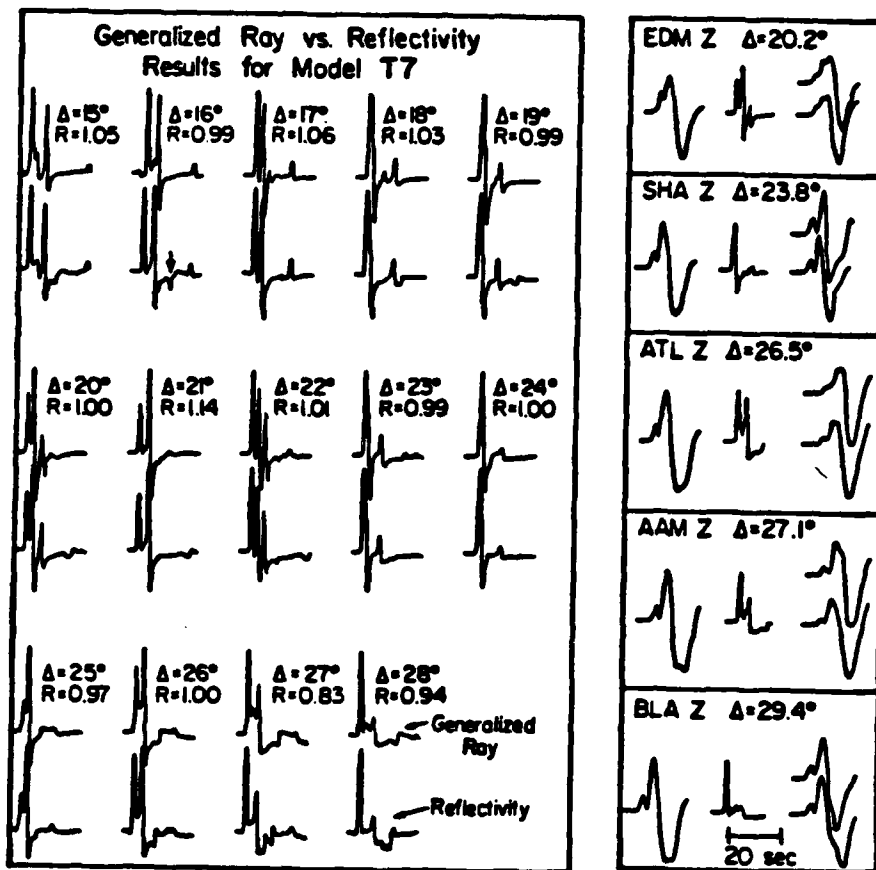


Fig 4.12 - (a) The slightly smoothed delta function responses from a reflectivity calculation (bottom) are compared to those from a generalized ray (top) for model T7. (b) First column contains the predicted waveshape due to the source only; second column is the delta function response of the model T7; third column is the convolution of the first two columns. The observed waveforms from the Borrego Mountain earthquake are on the top for comparison.

responses were generated by "Full Wave Theory" (see Cormier and Choy, 1981), with similar waveforms.

The vertical response for a dislocation source can be generated from $M(t)$ by assuming that the vertical radiation functions $C_j(p_0)$ etc., are nearly constant over the (p 's) involved, accordingly

$$(4.5) \quad W = \frac{M_0}{4\pi p_0} \frac{d}{dt} \left[D * \sum_{j=1}^3 A_j(\theta, \delta, \lambda) C_j(p_0) R_{PZ}(p_0) M(t) \right]$$

Similar approximations can be applied to generated pP , sP , and crustal multiples. With this approximation, the procedure becomes identical to the teleseismic expression (3.1) where the factor $(1/R)$ is replaced with a convolution of $M(t)$ followed by a derivative. Synthetics appropriate for the three fundamental faults are displayed in Figure 4.13. A synthetic seismogram appropriate for any arbitrary orientation can then be formed by taking a linear combination of these three as discussed earlier.

We can change the order of operations and generate the synthetic seismograms as if the $M(t)$ were a delta function as under the teleseismic assumption. The first column of Figure 4.12b corresponds to this order of operations. Convolving with the $M(t)$ produces the proper synthetic as given on the right of Figure 4.12b. The latter order of operations is generally used for studying upper-mantle structure since $M(t)$ is isolated from the other operations.

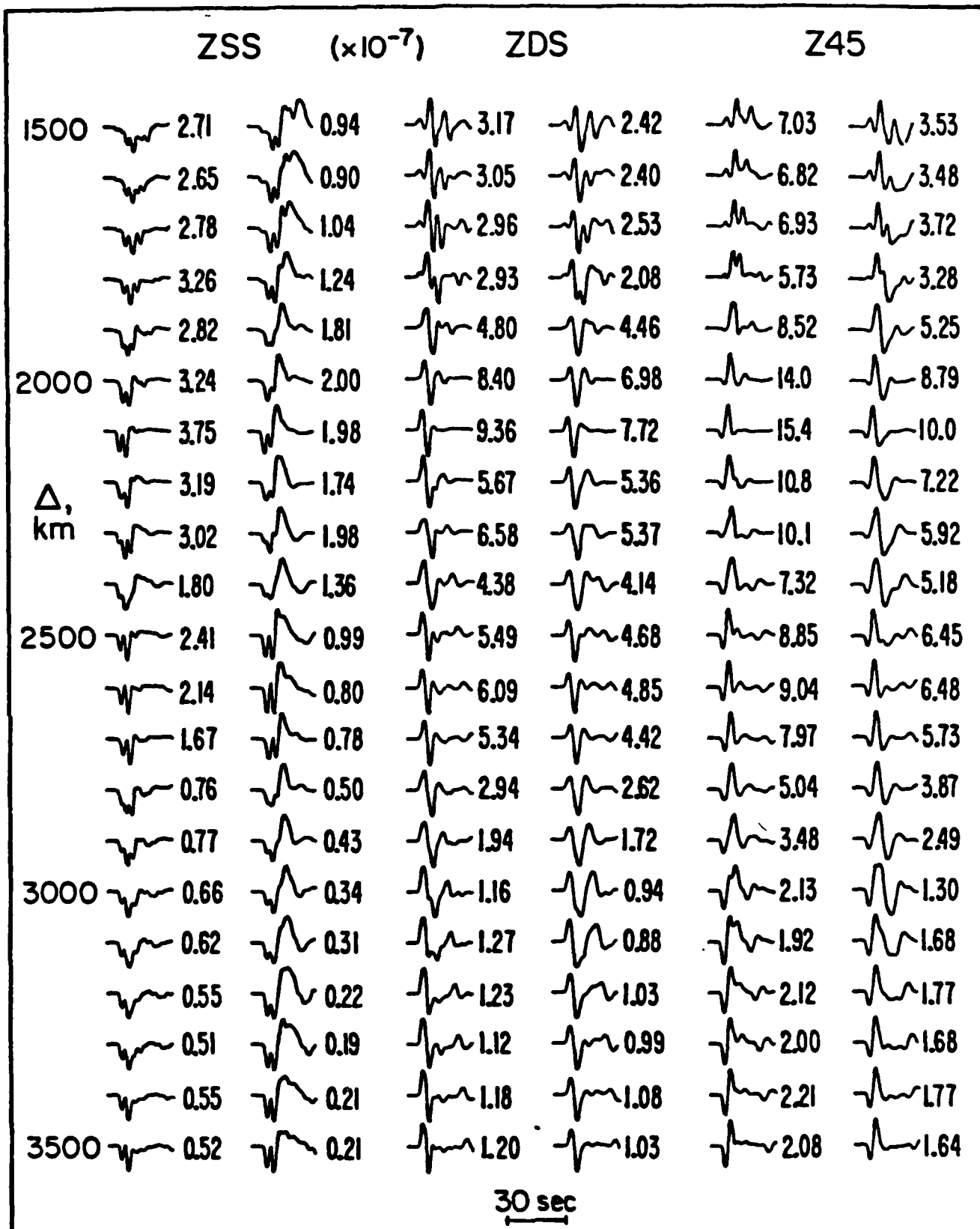


Fig 4.13 - Upper-mantle synthetics without and with instrument for the three fundamental orientations assuming a source depth of 8 km, $t^*=1$, and $\delta t_1 = \delta t_2 = \delta t_3 = 1$ for the source time history.

5. Discussion

In this review, we have presented a procedure for generating synthetic waveforms for body phases. For convenience, we divided the epicentral distances into teleseismic, regional, and local. At teleseismic distances, we showed that long period body phases from shallow earthquakes are coherent at neighboring stations and that the observed waveform could be decomposed in a manner that allows determination of faulting parameters. It appears that many events in

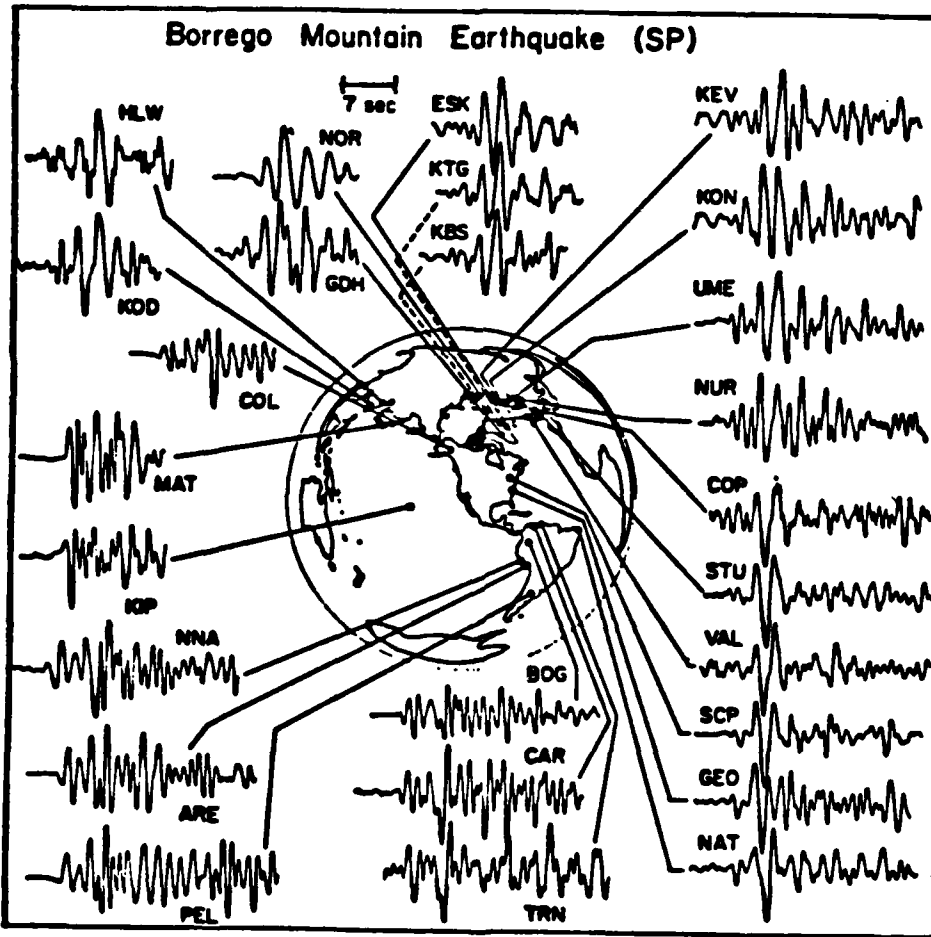


Fig 5.1 - Short-period P waveforms recorded at WWSSN stations. Note the coherence of the first several seconds of the waveforms from stations at similar azimuths. The star denotes the location of the earthquake (After Ebel and Helmberger, 1982).

the magnitude class 5.5 to 6.5 can be easily modeled at long periods by assuming point sources. This result should not be surprising since the signal wavelengths are long compared to the fault dimensions. On the other hand, the corresponding comparison between short period records at neighboring stations is much less coherent and complicated, see for example figure 5.1. Some success at explaining these records has been presented recently by Ebel and Helmberger (1982) by introducing complex faulting.

To model shorter periods requires that we generalize our point source procedures to treat finite faults as distributed point sources, see for example Langston (1978) and Heaton (1982). Following the latter technique we simply simulate rupturing on a fault plane by summing point sources with the proper timing, see figure 5.2. The procedure is made somewhat complicated by the presence of the free surface which requires summing pP, etc. Thus, teleseismic signals can show considerable variation with azimuth. Note that the long period records prove quite insensitive to the rupture properties in this simple case compared with the short periods. Conceptionally, we should be able to determine the time structure of the rupture process by simply matching short period waveform patterns and, indeed, this subject is being pursued vigorously. Unfortunately, at these periods the many idealistic assumptions involving the homogeneity of the mantle, simple flat layering near the source and receivers, planar fault planes, to name a few, begin to break down. Thus, the pattern recognition is not so obvious.

A simpler approach is to suppose that the rupture process can be simulated with some small number of point sources where each source has its particular time history. By modeling the long and short periods

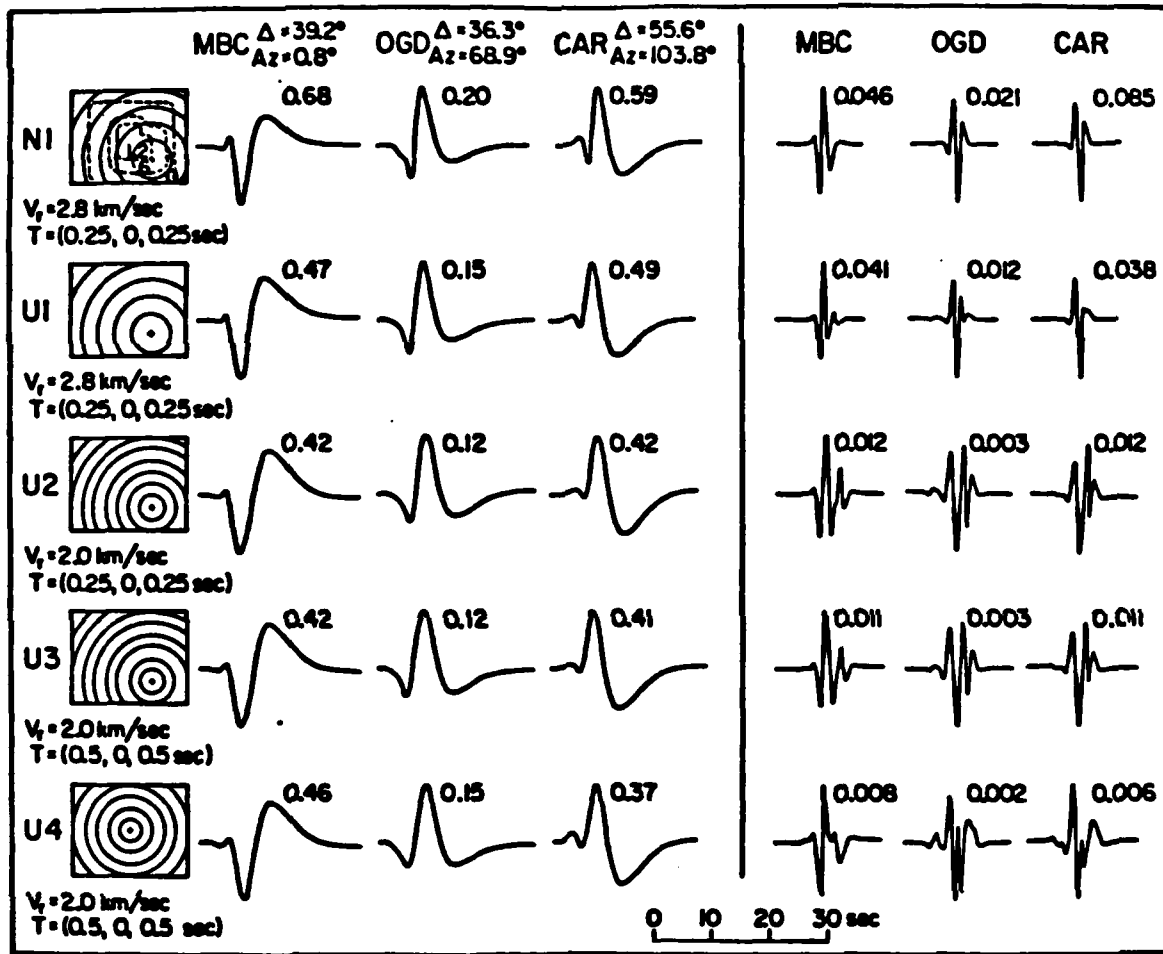


Fig 5.2 - Comparison of the short-period and long-period synthetics at the teleseismic stations for various fault models. The numbers are the amplitudes in micrometers calculated for the seismic moment of $.5 \times 10^{24}$ dyne-cm. The top row corresponds to a particular distribution of faulting appropriate for the Coyote earthquake where the dislocation is largest at the center and tapers down at the edges. The U1, U2, U3, and U4 models show uniform slip histories but with different rupture speeds (After Liu and Helmberger, 1982).

simultaneously with these few parameters, we can look for sub-structure. Such a procedure was tried recently by Wallace et al (1981b) on the Santa Barbara earthquake of 1978, see figure 5.3. These results indicate that on a smaller scale most earthquakes are indeed complex as suggested by Kanamori and Stewart (1978). The sharp jumps indicated in the time history of figure 5.3 are obviously important with respect to

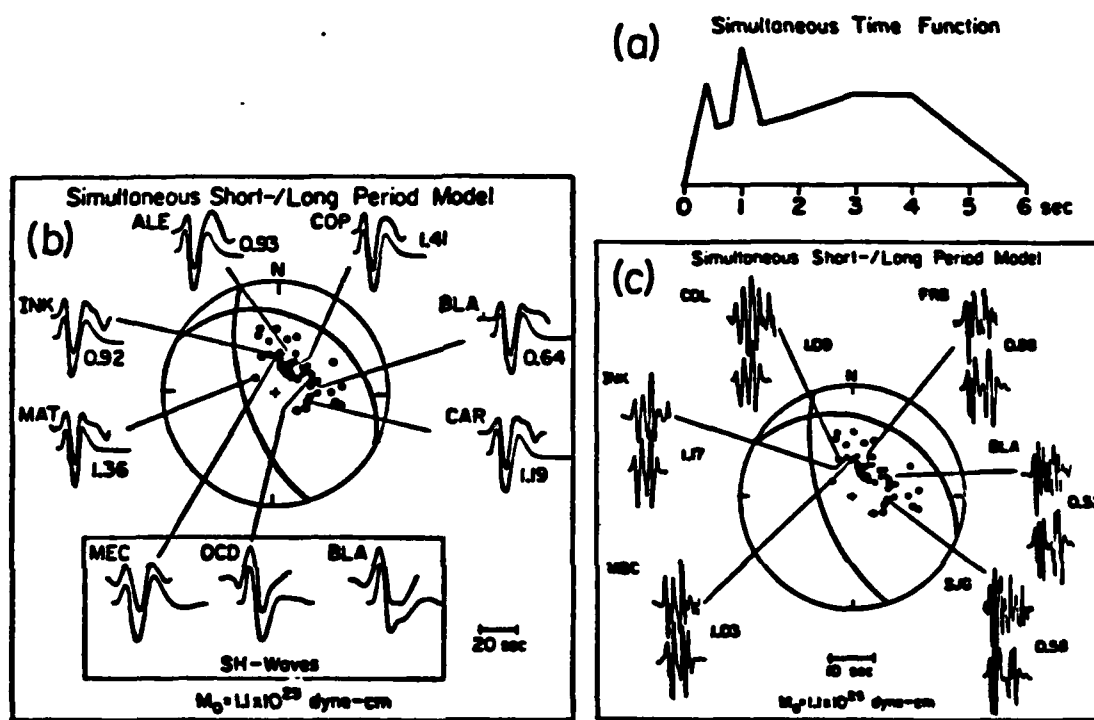


Fig 5.3 - Modelling experience obtained from studying the near- and far-field records of the 1978 Santa Barbara earthquake. a) displays the far-field time history for an effective point source; b) displays the fit of the long-period synthetics and data; c) displays the short period fit.

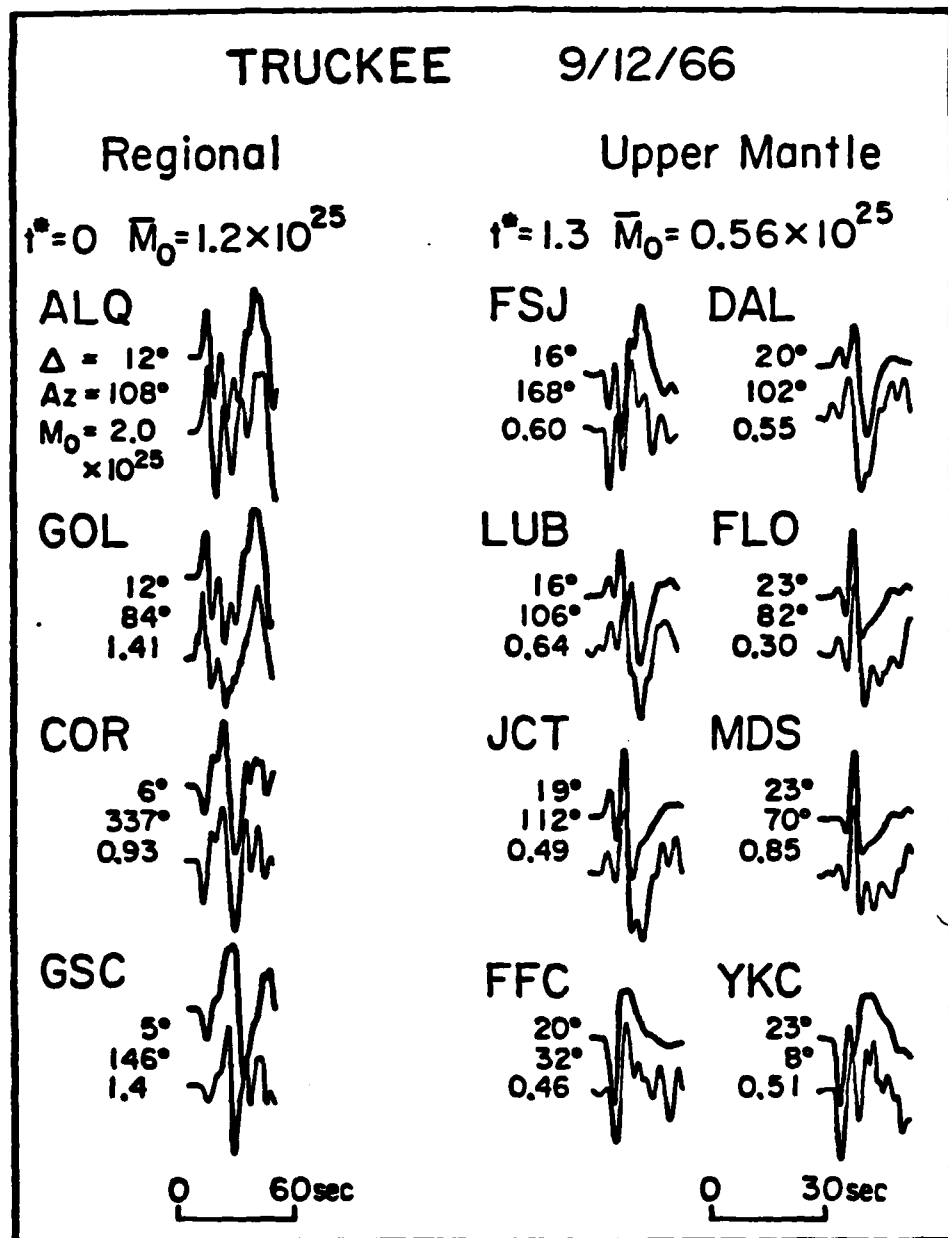


Fig 5.4 - Comparison of synthetics with waveform data at regional distances where the preferred model produces a ($\theta = 48^\circ$, $\lambda = 0^\circ$, and $\delta = 79^\circ$) (After Yao et al., 1982).

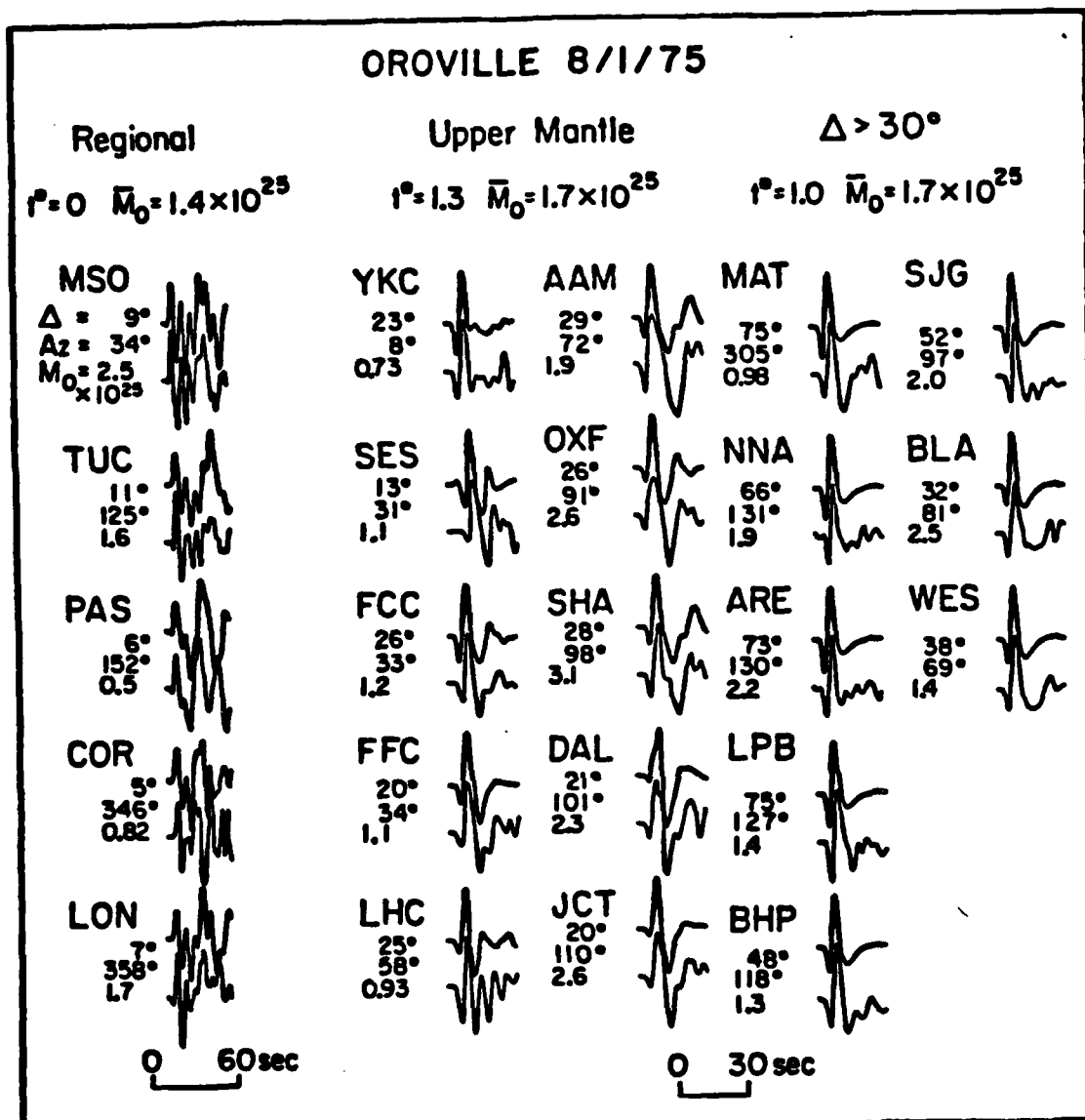


Fig 5.5 - Comparison of synthetics with waveform data at all ranges with preferred model ($\theta = 215^\circ$, $\lambda = -65^\circ$, and $\delta = 48^\circ$). Inversion results; with the 5 P_{ul} records exclusively are: ($\theta = 195^\circ$, $\lambda = -72^\circ$ and $\delta = 46^\circ$), 10 upper-mantle ranges exclusively are: ($\theta = 197^\circ$, $\lambda = -63^\circ$, and $\delta = 58^\circ$), 8 teleseismic waveforms exclusively are: ($\theta = 221^\circ$, $\lambda = -82^\circ$, and $\delta = 44^\circ$) (After Yao et al., 1982).

understanding the faulting mechanism, but their existence is particularly significant in estimating earthquake hazards. That is, the high frequency strong motions appear to be more strongly controlled by the jumps in the time history than by the overall duration (see Wallace *et al.*, 1981b; Ebel and Helmberger, 1982).

At ranges less than about 30° , we found that the body wave arrivals become multi-valued and some care needs to be taken to remove propagational features from source phenomena. Some progress in achieving this separation can be seen in figures 5.4 and 5.5 where we show that consistent estimates of the source orientation can be obtained at nearly any range. Note that there are no teleseismic waveforms for the Truckee event compared with the Oroville event, even though they are roughly the same strength. The reason is due to the difference in vertical radiation pattern as discussed earlier (see figure 3.2). How successful this analysis will be for other regions is not known but initial results look promising.

Acknowledgements

I would like to acknowledge the help of Gladys Engen, Jean Sauber, Z.X. Yao and Connie Sulentic who have helped assemble this manuscript. I would also like to thank the present and past graduate students who have helped to propel modeling into a respectable field and who have generated many of the figures displayed in this review.

Research supported by the Air Force Office of Scientific Research, AFOSR grant No. F49620-81-C-0008. Contribution No. 3790, Division of Geological and Planetary Sciences, California Institute of Technology, Pasadena, California 91125.

References

Bullen, K. E. (1965). An introduction to the theory of seismology, Chapter VIII, Third Edition, University Press, Cambridge.

Burdick, L. J. (1977). Broad-band seismic studies of body waves, Ph.D. Thesis, California Institute of Technology, Pasadena, California 91125.

Burdick, L. J. (1980). The mantle structure of North America and Europe, J. Geophys. Res., 86, 5926.

Burdick, L. J. and D. V. Helmberger (1978). The upper-mantle P velocity structure of the western United States, J. Geophys. Res., 83, 1699-1712.

Burdick, L. J. and G. R. Mellem (1976). Inversion of the body waves of the Borrego Mountain earthquake to the source mechanism, Bull. Seism. Soc. Am., 66, 1485-1499.

Burdick, L. J. and J. A. Orcutt (1978). A comparison of the generalized ray and reflectivity methods of waveform synthesis, Geophys. J., 58, p. 261.

Burridge, R., E. R. Lapwood and L. Knopoff (1964). First motions from seismic sources near a free surface, Bull. Seism. Soc. Am., 54, 1889-1913.

Carpenter, E. W. (1967). Teleseismic signals calculated for underground, underwater, and atmospheric explosions, Geophys., 32, 17-32.

Comnier, V. F. and G. L. Choy (1981). Theoretical body wave interactions with upper-mantle structure, J. Geophys. Res., 86,

1673-1678.

Ebel, J.E. and D.V. Helmberger (1982). P-wave complexity and fault asperities: The Borrego Mountain, California, Earthquake of 1968, Bull. Seism. Soc. Am., 72, pp.413-437.

Futterman, W. I. (1962). Dispersive body waves, J. Geophys. Res., 67, 5279-5291.

De Hoop, A. T. (1960). A modification of Cagniard's method for solving seismic pulse problems, Appl. Sci. Res., B8, 349-356.

Gilbert, F. J. and D. V. Helmberger (1972). Generalized ray theory for a layered sphere, Geophys. J., 27, 57-80.

Harkrider, D. G. (1976). Potentials and displacements for two theoretical sources, Geophys. J., 47, 97-133.

Harkrider, D. G. and D. V. Helmberger (1977). A note on non-equivalent quadrupole source cylindrical shear potentials which give equal displacements, Bull. Seism. Soc. Am., in press.

Haskell, N. A. (1964). Total energy and energy spectral density of elastic wave radiation from propagating faults, Bull. Seis. Soc. Am., 54, 1811-1831.

Heaton, T.H. and D.V. Helmberger (1977). A study of the strong ground motion of the Borrego Mountain, California, earthquake, Bull. Seism. Soc. Am., 67, 315-330.

Heaton, T.H. and D.V. Helmberger (1978). Predictability of strong ground motion in the Imperial Valley: Modeling the M=4.9, November 4, 1976, Brawley earthquake, Bull. Seism. Soc. Am., 68, 31-48.

Heaton, T.H. and D. V. Helmberger (1979). Generalized ray models of the San Fernando earthquake, Bull. Seism. Soc. Am., 69, 1311-1341.

Helmberger, D. V. (1968). The crust-mantle transition in the Bering Sea, Bull. Seism. Soc. Am., 58, 179-214.

Helmberger, D. V. (1974). Generalized ray theory for shear dislocations, Bull. Seism. Soc. Am., 64, 45-64.

Helmberger, D. V. and G. R. Engen (1980). Modeling the long-period body waves from shallow earthquakes at regional ranges, Bull. Seism. Soc. Am., 70, 1699-1714.

Helmberger, D. V. and D. G. Harkrider (1978). Modeling earthquakes with generalized ray theory, Proceedings of IUTAM Symposium: Modern Problems in Elastic Wave propagation, J. Miklowitz and J. Achenbach, eds. John Wiley and Sons, New York.

Helmberger, D. V. and S. D. Malone (1975). Modeling local earthquakes as shear dislocations in a layered half-space, J. Geophys. Res., 80, 4881-4888.

Helmberger, D.V. (1973). On the structure of the low-velocity zone, Geophys. J., 34, 251-263.

Hron, F. and E. R. Kanasewich (1971). Synthetic seismograms for deep seismic sounding studies using asymptotic ray theory, Bull. Seism. Soc. Am., 61, 1169-1200.

Hong, T. L. and D. V. Helmberger (1977). Generalized ray theory for dipping structure, Bull. Seism. Soc. Am., 67, 995-1008.

Hong, T. L. and D. V. Helmberger (1978). Glorified optics and wave propagation in nonplanar structure, Bull. Seism. Soc. Am., 68,

1313-1330.

Kanamori, H. and G.S. Stewart (1978). Seismological aspects of the Guatemala earthquake of February 4, 1976, J. G. R., 83, 3427-3434.

Knopoff, L. and F. Gilbert (1959). Radiation from a strike-slip fault, Bull. Seism. Soc. Am., 49, 163-178.

Lamb, H. (1904). On the propagation of tremors over the surface of an elastic solid, Phil. Trans. Roy. Soc. London, A203, 1-42.

Langston, C. A. (1978). The February 9, 1971 San Fernando earthquake: A study of the source finiteness in teleseismic body waves, Bull. Seism. Soc. Am., 68, 31-48.

Langston, C. A. and D. E. Blum (1977). The April 29, 1965 Puget Sound earthquake and the crustal and upper-mantle structure of western Washington, Bull. Seism. Soc. Am., 67, 693-711.

Langston, C. A. and R. Butler (1976). Focal mechanism of the August 1, 1975 Oroville earthquake, Bull. Seism. Soc. Am., 66, 1111-1120.

Langston, C. A. and D. V. Helmberger (1975). A procedure for modeling shallow dislocation sources, Geophys. J. R. Astron. Soc., 42, 117-130.

Liu, H.L. and D.V. Helmberger (1982). The near-source ground motion of the August 6, 1979 Coyote Lake, California, earthquake, in press.

Madariaga, R. (1976). Dynamics of an expanding circular fault, Bull. Seism. Soc. Am., 66, 639-666.

Minster, J. B. (1978). Transient and impulse responses of a

one-dimensional linearly attenuating medium, II. A parametric study, Geophys. J., 52, 503-524.

Spencer, T. (1960). The method of generalized reflections and transmission coefficients, Geophys., 25, 625-641.

Stewart, G. S. and D. V. Helmberger (1981). The Bermuda earthquake of March 24, 1978, J. Geophys. Res., 86, 7027-7036.

Strick, E. (1959). Propagation of elastic wave motion from an impulsive source along a fluid-solid interface, Parts II and III, Phil. Trans. Roy. Soc. London, Series A, 251, 465-523.

Tsai, Y. B. and K. Aki (1970). Source mechanism of the Truckee, California earthquake of September 12, 1966, Bull. Seism. Soc. Am., 60, 1199-1208.

Wallace, T.C. and D.V. Helmberger (1982). Determining source parameters of moderate-size earthquakes from regional waveforms (in preparation).

Wallace, T. C., D. V. Helmberger, and G. R. Mellman (1981a). A technique for the inversion of regional data in source parameter studies, J. Geophys. Res., 86, 1679-1685.

Wallace, T.C., D.V. Helmberger and J.E. Ebel (1981b). A broad band study of the 13 August 1978 Santa Barbara earthquake, Bull. Seism. Soc. Am., 71, 1701-1718.

Yao, Z.X., T.C. Wallace and D.V. Helmberger (1982). Earthquake source parameters from sparse bodywave observations. Earthquake Notes, 53, 38.

Appendix A. Generalized Ray Theory

The method of generalized ray theory allows one to construct the solution of a seismic boundary value problem by inspection. The method was first introduced to the seismic community by Spencer (1960). The idea can be easily understood by working through a simple example, namely the sandwiched fluid layer problem (see figure A1). The solution

Fig A1 - Schematic of the geometric setup with a sandwiched fluid layer.

Source	Receiver
★	○
h	ϕ_1, ρ_1, a_1
Th	ϕ_2, ρ_2, a_2
	ϕ_3, ρ_3, a_3

in terms of potentials assuming the asymptotic form becomes

$$\bar{\phi}_1(x, z, s) = \sqrt{\frac{2}{\pi rs}} \operatorname{Im} \int \frac{\sqrt{p}}{\eta_1} e^{-s(pr+\eta_1|z-h|)} + A(p)e^{-s(pr+\eta_1(z+h))} dp$$

$$\bar{\phi}_2(x, z, s) = \sqrt{\frac{2}{\pi rs}} \operatorname{Im} \int \frac{\sqrt{p}}{\eta_1} e^{-s(pr+\eta_1(z+h))} [Be^{-s\eta_2 z} + Ce^{+s\eta_2 z}] dp$$

$$\bar{\phi}_3(x, z, s) = \sqrt{\frac{2}{\pi rs}} \operatorname{Im} \int \frac{\sqrt{p}}{\eta_1} e^{-s(pr+\eta_1(z+h))} [D(p)e^{+s\eta_3 z}] dp$$

with the simple boundary conditions on continuity of vertical stress and displacement across the interfaces, that is

$$\rho_1 \phi_1 = \rho_2 \phi_2 \\ z=0$$

$$\frac{d\bar{\phi}_1}{dz} = \frac{d\bar{\phi}_2}{dz}$$

$$\rho_2 \phi_2 = \rho_3 \phi_3 \\ z=-Th$$

$$\frac{d\bar{\phi}_2}{dz} = \frac{d\bar{\phi}_3}{dz}$$

These four equations are used to solve for the four unknowns A, B, C, and D. Substituting the $\bar{\phi}_1$ into the boundary conditions, we obtain

$$A = \left[\frac{R_{12} + R_{23} e^{-2Th \sin^2_2}}{1 + R_{12} R_{23} e^{-2Th \sin^2_2}} \right]$$

where

$$R_{12} = \frac{\rho_2 \eta_1 - \rho_1 \eta_2}{\rho_2 \eta_1 + \rho_1 \eta_2}, \text{ and } R_{23} = \frac{\rho_3 \eta_2 - \rho_2 \eta_3}{\rho_3 \eta_2 + \rho_2 \eta_3}$$

Note that as $Th \rightarrow 0$

$$A = \frac{\rho_3 \eta_1 - \rho_1 \eta_3}{\rho_3 \eta_1 + \rho_1 \eta_3}$$

and as $Th \rightarrow \infty$, $A = R_{12}$, as expected.

Next, we use the identity

$$\frac{1}{1+x} = (-1)^n x^n$$

and expand A to obtain a series solution

$$A = R_{12} + \sum_{n=1}^{\infty} (-1)^{n+1} R_{23}^n R_{12}^{n-1} (1-R_{12}^2) e^{-2Th \sin^2_2} n$$

Rewriting $\bar{\phi}_1(r, z, s)$ as

$$\bar{\phi}_1 = \bar{\phi}_{\text{direct}} + \bar{\phi}_{\text{reflected}} + \bar{\phi}_n$$

We have

$$\bar{\phi}_n(r, z, s) = \sqrt{\frac{2}{\pi rs}} \text{ Im} \int \sqrt{\frac{2}{\eta_1}} [(-1)^{n+1} R_{23}^n R_{12}^{n-1} (1-R_{12}^2)] e^{-s(pr+\eta_1(z+h)-2Th \sin^2_2)} dp$$

or

$$\bar{\phi}_n(r, z, s) = \sqrt{\frac{2}{\pi rs}} \text{ Im} \int \sqrt{\frac{2}{\eta_1}} f_n(p) e^{-s(pr+\eta_1(p))} dp$$

with

$$f_n(p) = R_{23}^n R_{12}^{n-1} (1-R_{12}^2)(-1)^{n+1}$$

$$g_n(p) = n_1(z+h) + 2Thn_n_2$$

Each value of (n) corresponds to a particular ray, for example
with n = 1 we obtain

$$f_1(p) = R_{23}(1-R_{12}^2)(-1) = T_{12}R_{23}T_{21}$$

$$g_1(p) = 2Thn_2 + n_1(z+h)$$

where the identity $(1-R_{12}^2) = T_{12}T_{21}$ was used,

$$T_{12} = \frac{2n_1\rho_1}{\rho_2n_1 + \rho_1n_2}$$

and

$$T_{21} = \frac{2n_2\rho_2}{\rho_2n_1 + \rho_1n_2}$$

and, similarly, for n = 2 we obtain

$$f_2(p) = T_{12}R_{23}R_{21}R_{23}T_{21}$$

$$g_2(p) = 4Thn_2 + n_1(z+h).$$

Thus, the solution is built-up by adding up the various rays which can be determined by inspection.

We can check our solution and resulting code by generating the step response of a sandwiched layer in the limit of small thickness and compare the results with the solution with no layer, see figure A2. Next, we examine the case where we go beyond critical angle so that the receiver is in the geometric shadow and investigate tunneling. In this case, the layer is too thin to support a head wave and, thus, the strong interference effects introduced by the multiples. The solution can be written

$$\bar{\Phi}_3(r, z, s) = \sqrt{\frac{2}{\pi s}} \operatorname{Im} \int \frac{\sqrt{2}}{\eta_1} e^{-s(pr + \eta_1 h + \eta_2 Th + \eta_3 H)} D dp$$

where

h = distance from the layer to receiver

H = distance from the layer to source

Th = layer thickness

$$D = (T_{12} T_{23}) / (1 + R_{12} R_{23} e^{-2Th\eta_2 s})$$

expanding D in a series yields the ray expansion and the multiples displayed in figure A2. When the layer is too thin to support head waves, we can obtain a useful approximation by noting that

$$\lim_{Th \rightarrow 0} D = T_{13} = 1$$

Thus, the only effect of the layer on the solution is in the contour

$$t = pr + \eta_1(h + H) + Th\eta_2$$

Essentially, the contour moves off of the real p -axis at $p = 1/\alpha_2$ and, thus, no longer will there be a square-root singularity at the direct arrival time but slightly smoothed depending on the thickness. That is, the height of the steps given in figure A2 corresponds to the same amplitude of the steps with no layer. However, the rise-time of these steps are no longer sharp. Thus, when these step responses are used to generate synthetics, they filter out the high-frequencies or short periods. The effect is nearly identical to the Q-operators

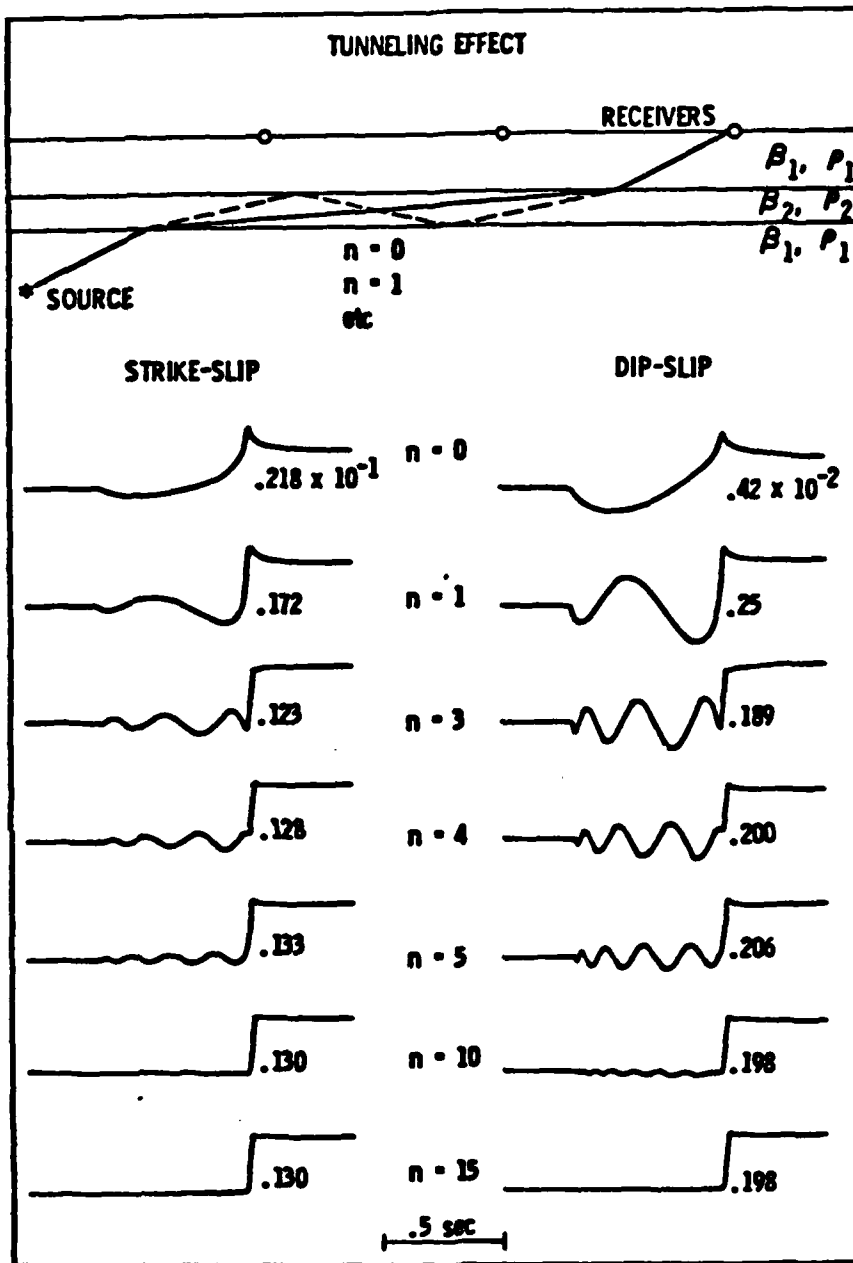


Fig A2 - Numerical step response of tunneling. The source depth is 3 km with a 20 km source-receiver separation. Seismic parameters are $\rho_1 = 2.3 \text{ gm/cm}^3$, $\beta_1 = 2.02 \text{ km/sec}$, and $\rho_2 = 2.4 \text{ gm/cm}^3$, $\beta_2 = 2.31 \text{ km/sec}$, with a barrier thickness of 10 meters. Relative peak amplitudes are given for each case. n indicates the number of rays included in the sum.

discussed earlier.

The technique of constructing a solution by simply adding up rays that have traversed the various layers with some specified mode of propagation is called the method of "Generalized Reflection and Transmission Coefficients." The coefficients for the solid/solid interface are somewhat more complicated because of the possible mode changes from P to SV, etc., but the procedure is basically the same. The generalized reflection and transmission coefficients used in this paper are given by Helmberger (1968).

Another concept commonly used in GRT is that of receiver functions. Note that we have been working with potentials throughout these notes. Essentially, we start with a source potential and propagate it to some location by applying the proper product of T and R coefficients. At the receiver we need to convert this potential into a displacement or some measurable quantity. In a whole space, the displacements can be obtained by simply performing the derivatives defined by equation (2.24). On a free surface the conversion from potential to displacement becomes more complicated, see figure A3. The proper way to satisfy the boundary conditions is to take the limit as Z goes to zero and sum the three arrivals since the travel paths coincide and label the results "receiver functions." The results for incoming P-waves are:

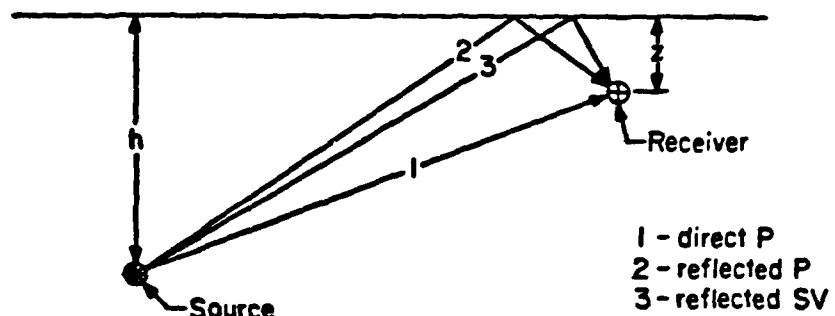
$$R_{PZ} = 2\eta_a(\eta_b^2 - p^2)/B^2 D(p)$$

$$R_{PR} = -4\eta_a\eta_bp/B^2 D(p)$$

where

$$D(p) = (\eta_b^2 - p^2) + 4p^2\eta_a\eta_b$$

Fig A3 - Schematic showing the interaction of the three arrivals that form the receiver function.



The second subscript indicates component, namely Z for vertical and R for radial. The results for incoming SV-waves are:

$$R_{SZ} = 4pn_a n_b / \beta^2 D(p)$$

$$R_{SR} = 2n_b(n_b^2 - p^2) / \beta^2 D(p)$$

Table 1
Crustal Model

PVEL	SVEL	Density	Layer Thickness
6.2	3.5	2.7	32.0
8.2	4.5	3.4	